THESIS FOR THE DEGREE OF DOCTOR OF PHILOSOPHY IN SOLID AND
STRUCTURAL MECHANICS

Image-based numerical modelling of heterogeneous materials

ROBERT MICHAEL AUENHAMMER

Department of Industrial and Materials Science
Division of Material and Computational Mechanics
CHALMERS UNIVERSITY OF TECHNOLOGY

Göteborg, Sweden 2023

Image-based numerical modelling of heterogeneous materials
ROBERT MICHAEL AUENHAMMER
Department of Industrial and Materials Science
Division of Material and Computational Mechanics
Chalmers University of Technology

Abstract

In science there has always been a desire to visualise the invisible. Since the discovery of X-rays in 1895, imaging research has made remarkable progress. Nowadays, state-of-the-art technology allows to visualise the micro-structure of objects in three dimensions.

However, merely visualising the structure is often insufficient. The quantitative information regarding morphology and structure is of great interest. Therefore, in addition to significant advancements in X-ray image acquisition and three-dimensional reconstruction, image analysis has become an active research field in recent years. Modern image analysis methods enable to extract even invisible information from image data.

The heterogeneous micro-structure of composites imposes advanced material characterisation as even for the largest composite structures, such as wind turbine blades or airplane wings, the material properties are dictated on the micro-scale. Image-based modelling offers exceptional capabilities in analysing the micro-structure at the fibre level and numerically predicting material behaviour even at larger scales. However, image-based modelling is a complex process and all work-steps must be in line with the final modelling goal. Therefore, X-ray computed tomography aided engineering has been introduced to emphasise the importance of a holistic point of view on the image-based modelling process.

The developed X-ray computed tomography aided engineering methodology has been developed based on micro X-ray computed tomography scans for non-crimp fabric glass-fibre reinforced composites. It is demonstrated that local fibre orientations and fibre volume fractions can be accurately imaged and transferred onto a finite element model. Thereby, the tensile modulus of the scanned samples can be accurately predicted and possible stress concentration regions detected.

However, conventional micro X-ray computed tomography presents a major drawback. Achieving the required high resolutions to visualise carbon or glass fibres, typically ranging between 5 to $20\,\mu m$, limits the scanning field of view, which remains in the millimetre range. This drawback is overcome with new approaches in image-based modelling involving advances in imaging and image analysis. Therefore, targeted approaches for accurate image-based modelling are presented which increase the possible scanning field-of-view of fibrous composites by up to three to six orders of magnitude.

Keywords: Composites, X-ray computed tomography, image analysis, image-based modelling

Avancez

PREFACE

This project has been carried out from June 2019 until September 2023. The first three years of this project have been set up within the Intensive Training Network Mummering (MUltiscale, Multimodal and Multidimensional imaging for EngineeRING) project (Grant number 765604), as part of the Marie Skłodowska-Curie Actions HORIZON programme funded by European Commission. In the project the fifteen participating PhD students were trained in all aspects of tomography. At the same time a large European/International network with many research and industrial collaborations has been created. The remaining part of this work has been financed by Fordonsstrategiska Forskning och Innovation (Grant number 2021-05062), where the progress made in image-based modelling during the Mummering project phase could be seamlessly employed to effectively characterise intricate natural fibre composites intended for industrial applications.

Thesis

This thesis consists of an extended summary and the following appended papers:

Paper A
R. M. Auenhammer, L. P. Mikkelsen, L. E. Asp, B. J. Blinzler. Automated X-ray computer tomography segmentation method for finite element analysis of non-crimp fabric reinforced composites. Composite Structures 256 (2021), 113136.

Paper B
R. M. Auenhammer, L. P. Mikkelsen, L. E. Asp, B. J. Blinzler. X-ray tomography based numerical analysis of stress concentrations in non-crimp fabric reinforced composites - assessment of segmentation methods. IOP Conference Series: Materials Science and Engineering 942 (2020), 012038.

Paper C
R. M. Auenhammer, N. Jeppesen, L. P. Mikkelsen, V. A. Dahl, B. J. Blinzler, L. E. Asp. Robust numerical analysis of fibrous composites from X-ray computed tomography image data enabling low resolutions. Composites Science and Technology 224 (2022), 109458.

Paper D
R. M. Auenhammer, A. Prajapati, K. Kalasho, L. P. Mikkelsen, P. Withers, L. E. Asp, R. Gutkin. Fibre orientation distribution function mapping for short fibre polymer composite components from low resolution/large volume X-ray computed tomography. Submitted for international publication

Paper E
R. M. Auenhammer, J. Kim, C. Oddy, L. P. Mikkelsen, M. Stampanoni, F. Marone, L. E. Asp. X-ray scattering tensor tomography based finite element modelling of fibre reinforced composites. Submitted for international publication

Paper F
R. M. Auenhammer, N. Jeppesen, L. P. Mikkelsen, V. A. Dahl, L. E. Asp. X-ray computed tomography data structure tensor orientation mapping for finite element models — STXAE. Software Impacts 11 (2022), 100216.

The appended papers were collaboratively prepared with co-authors. The author of this thesis was responsible for the major progress of the work, e.g., planning scans, writing code, running simulations, post-processing and writing. The image analysis code used in **Paper C, D and F** has been developed at DTU Compute.

Other peer-reviewed publications related to thesis but not appended - open access link added

Publication I S. Duan, M. Cattaruzza, V. Tu, R. M. Auenhammer, F. Liu, R. Jänicke, M. Johansson, L. E. Asp. 3D reconstruction and computational analysis of a structural battery composite porous electrolyte. Communications Materials 4 (2023), 49. DOI: 10.1038/s43246-023-00377-0.

Publication II R. M. Auenhammer, L. P. Mikkelsen, L. E. Asp, B. J. Blinzler. Dataset of non-crimp fabric reinforced composites for an X-ray computer tomography aided engineering process. Data in Brief 33 (2020), 106518. DOI: 10.1016/j.dib.2020.106518.

Published code

Publication III R. M. Auenhammer, N. Jeppesen, L. P. Mikkelsen, V. A. Dahl, L. E. Asp. STXAE - X-ray computed tomography data structure tensor orientation mapping for finite element models. Code Ocean (2021), 4407802. DOI: 10.24433/CO.4407802.v1.

Publication IV N. Jeppesen, R. M. Auenhammer, L. P. Mikkelsen. Structure tensor analysis and 2D finite element integration pointwise material orientation mapping. Code Ocean (2022), 4407802. DOI: 10.24433/co.9768579.v1

Publication V R. M. Auenhammer, C. Oddy, J. Kim, L. P. Mikkelsen. X-ray scattering tensor tomography-based finite element modelling. Code Ocean (2023), 6741464. DOI: 10.24433/CO.6741464.v1

CONTENTS

Part I
Extended Summary

<div align="right">

CHAPTER **1**

</div>

<div align="right">

Introduction

</div>

This chapter provides a background of the studied materials in this project and the approaches necessary to investigate those materials. From this basis the objectives for this research project are defined.

We are consuming too many resources on this planet. This includes water, agricultural land, phosphor, sand, fossil hydrocarbons, to name some of the most important. Every building we build, every product we buy, every meal we eat comes from resources on this planet and creates therefore an impact on the environment. Given the still growing world population and the problems arising with climate change, an efficient use of resources and materials is indispensable. Intelligently designed fibre reinforced composites can be of great benefit for a more sustainable material production, use and end-of-life.

1.1   Fibre reinforced composites

For fibre reinforced composites the fibre scale is dominating. Even for 100 m long wind turbine blades, stiffness, strength and fatigue properties are defined on the fibre level [1]. There are numerous parameters that affect those mechanical properties, e.g. fibre-matrix bonding [2], composite curing profile [3], void content [4], fibre volume fraction [5]. Central, however, is the fibre orientation [6]. One reason for the stiffness/weight advantage of fibre reinforced composites lies in the anisotropy of the material. The composite is less compliant along the fibre direction. Therefore, composites are usually designed with fibres oriented along known loading directions. If during manufacture a deviation from the

designed fibre orientation occurs, the composite is significantly weakened. In case the composite needs to bear multi-axial loading directions three-dimensional, woven fibre composites are a popular choice given the flexibility to tailor the mechanical properties [7, 8].

In the first part of this research project mainly non-crimp fabric reinforced glass fibre composites have been studied. The methods developed on non-crimp fabric reinforced composites have then been applied on pultruded, injection-moulded, and prepreg composites with different fibre types, e.g. natural, glass or carbon fibres.

Non-crimp fabric reinforced composites have been originally developed for large structural parts in marine and aeronautical applications [9] and are nowadays also used in automotive and wind industrial applications [10]. They are usually manufactured with resin transfer moulding [11] or vacuum infusion [12]. Non-crimp fabric reinforced composites are characterised by high in-plane and poor out-of-plane stiffness properties, compared to other fabric composites, e.g., woven composites. The high in-plane stiffness originates from practically straight fibre bundles with a high local fibre volume fraction, which are embedded in a polymer matrix. This layup yields resin-rich areas with no fibres present. Often the unidirectional bundles are kept together by stitching treads and backing bundles, which are oriented in the transverse direction. Both features have shown to introduce stress concentrations [13] which are disadvantageous during fatigue loading [14, 15].

In addition to non-crimp fabric reinforced composites with continuous fibres, short glass and carbon fibre reinforced polymers are also studied. Possible manufacture methods are extrusion and injection moulding. During those processes the fibres in the mould are shortened, which has a significant influence on the composite strength [16]. Injection-moulded composites are especially popular in mass production, e.g., in the automotive industry, due to injection moulded part's unparalleled cost-effectiveness for a high stiffness to weight ratio [17]. During the injection moulding process the fibres are predominantly aligned along the mould flow direction [18] resulting in a globally non-uniform but locally uniform fibre orientation distribution [19].

Another group of fibres with increasing popularity is natural fibres. This is the umbrella term for a large variety of fibre types, e.g., kenaf, flax, jute, hemp, silk, cotton. They offer superior sustainability properties, since they require less energy for production than for example carbon fibres [20], and they are biodegradable [21]. Further, their stiffness-to-weight ratio can be higher than for glass fibres [22] and they excel in noise absorption properties [23]. However, natural fibres also have some downsides. They are neither uniform in shape [24] nor easy to align uniformly [25]. Additionally, they are characterised by anisotropic stiffness properties [26], a greater variability in their properties [27, 28], and a tendency of hygroscopic swelling, which leads in turn to radial stresses at the interface between fibre and matrix [29].

1.2   X-ray imaging

X-rays have a short wavelength in the order of $10\,\mathrm{nm}$ and the application resolutions range between $50\,\mathrm{nm}$ to $10\,\mathrm{mm}$. The development of X-ray imaging started with the discovery of X-rays by Willhelm Röngten 1896, with the basic principle that an X-ray

(a) *Absorption-based X-ray imaging*

(b) *Scattering-based X-ray imaging*

(c) *Refraction-based X-ray imaging*

(d) *Phase-shift-based X-ray imaging*
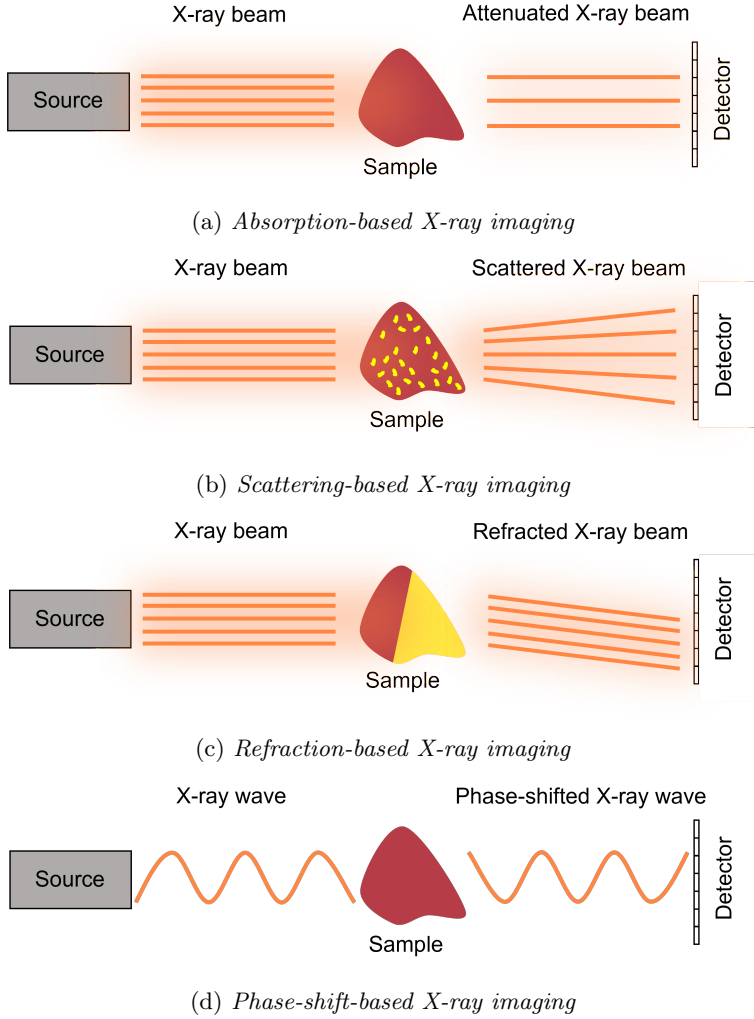
Figure 1.1: *Schematic drawing of different popular X-ray imaging technologies. Here, the character of light being both particle and wave is exploited.*

beam is attenuated on its propagation through matter due to absorption and scattering [30]. Since then the options for X-ray imaging have become manifold. Nowadays, the morphology of an object can be studied with micro computed tomography, while the structure can be also analysed by X-ray scattering or refraction. Although, the most common approach is still absorption-based micro computed tomography [31, 32] (Figure 1.1a), small [33, 34, 35] and wide [36, 37] angle X-ray scattering (Figure 1.1b), refraction [38, 39] (Figure 1.1c) or phase-contrast [40, 41] (Figure 1.1d) imaging have become increasingly popular during the last years. However, imaging continues to face certain

| (a) *2 projections* | (b) *4 projections* | (c) *8 projections* | (d) *16 projections* |
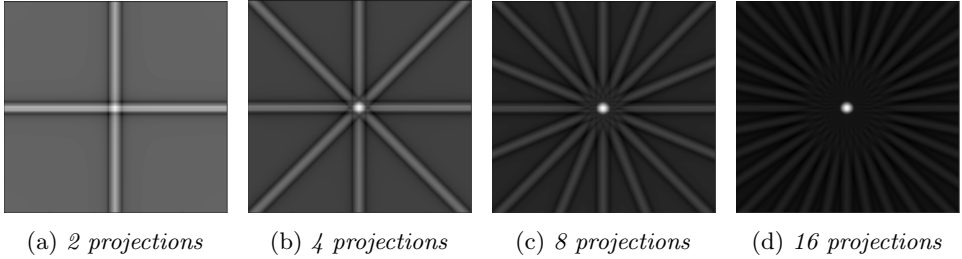
Figure 1.2: *Reconstruction of a point with the method Filtered Backprojection with 2, 4, 8 and 16 projections with the ASTRA Tomography Toolbox [44]. More projections further increase the quality of the reconstruction.*

limitations. The desired level of resolution frequently constrains the possible field of view, while achieving high-resolution scans results in long acquisition times and generates large data-sets. Additionally, obtaining satisfactory contrasts between various phases within a sample can be a challenging task. However, active research and growing popularity of imaging indicate that the benefits often outweigh the challenges [42].

1.2.1 Micro X-ray computed tomography

X-ray tomography scanners consist of an X-ray source, usually a rotating sample and a stationary two-dimensional detector. The X-ray source for lab-based systems emits a cone beam with a wide energy spectrum, synchrotron sources on the other hand are characterised by parallel beams and a defined small energy spectrum. From its original application field in medical imaging in the 1960s active research in computed tomography has covered the demand for three-dimensional imaging in various fields in recent decades. Improved and affordable computed tomography scanners together with the progress in the consecutive processes has made the technology broadly applicable for medical as well as industrial and academic utilisation across several fields [43].

The X-rays passing through the sample to be scanned are attenuated due to the photoelectric effect. The photons that passed through are measured on a two-dimensional detector. The X-ray attenuation follows the Beer-Lambert's law (Equation 1.1) where I represents the recorded x-ray intensity, I_0 the initial x-ray intensity, x the path length of propagated X-rays and μ the linear attenuation coefficient of the material [45].

$$I = I_0 e^{-\mu x} \tag{1.1}$$

The linear attenuation coefficient μ (Equation 1.2) itself depends on the density of the material ρ, the atomic number Z, the initial energy of the X-ray photons E and a constant K.

$$\mu = K\rho\frac{Z}{E} \tag{1.2}$$

For different materials different grey-scale values (typically expressed in 16 bits between 0 and 65,536) in the two-dimensional projections will be seen on the detector. The detector

is divided into a finite amount of pixels that transfer the photon signal into an electric signal. By rotating either the object or the source and detector an information about the size and position in three dimensions can be added. Therefore, the two-dimensional projections need to be transformed back to a three-dimensional image; the so-called reconstruction (Figure 1.2). Generally applies, the higher the amount of projections the better the original object, a circular dot in this figure, is reconstructed. The inverse mathematical problem of reconstruction can be either solved analytically or iteratively [46]. Also machine learning approaches have become a common choice and have enabled many new applications [47, 48, 49].

1.2.2 Small angle X-ray scattering

Decoded local small-angle X-ray scattering (SAXS) signals allow the non-destructive analysis of micro-structure orders of magnitude smaller than the voxel size [50]. This method uses a regular X-ray beam as conventional micro computed tomography [51], but the detector is placed further away to enable an angle enlargement of the small angle scattered X-rays. At modern synchrotron beamlines, sample to detector distances can easily reach 10 m [52]. Scattering signals can be acquired in vacuum [53] or free air [54] depending on the set-up.

With the use of phase modulator X-ray optics, consisting of circular grating arrays, placed between sample and detector, circular fringes are formed at the detector [55]. The difference in the circular fringes with and without the sample in the beam path allows to extract an omidirectional two-dimensional scattering signal [56]. To obtain three-dimensional information the measurement is repeated at different angular poses. A scattering tensor representing the three-dimensional scattering information is then voxel-wise tomographically reconstructed [57]. The circular gratings induced omidirectional scattering signal significantly shortens the acquisition time compared to other small-angle X-ray scattering methods [58]. This allows to time-efficiently scan and analyse the micro-structure of samples on the centimetre scale.

1.3 Image analysis

Image analysis is often described as bottleneck in the workflow from acquisition to modelling [59, 60]. With enough experience it is nowadays fairly easy to obtain a three-dimensional image data-set of acceptable quality. However, it is often difficult to extract quantitative information from the image data-set for accurate modelling. One issue is large data sizes. Data sizes in the range between 10 to 100 GB can be easily produced. The processing time, depending on the method, can reach several hours for a 10 GB data-set [61].

Naturally, it is often tried to create an image analysis algorithm that mimics the human eye. In fact the capabilities of the human eye, although being subjective and bias, are hard to mimic. In other words the human eye excels in segmenting objects which pose a difficult task for a segmentation algorithm. In the image analysis of scanned patients the trend goes to deep neural networks that are trained by the best radiologists in the field [62, 63]. The outcome will never be better than the capabilities of the radiologists

that have trained the network, but the likeliness of a misdiagnosis is reduced. However, there are new image analysis codes that go beyond the capabilities of the human eye. The structure tensor code by Jeppesen et al. [64] for example is able to estimate dominant fibre orientations for voxel-sizes up to three times the fibre diameter. This is not possible for the human eye.

With the large popularity of X-ray computed tomography also many commercial and academical segmentation solutions have been introduced. One of the most common commercial products for materials is Avizo [65] from Thermo Fisher, but there are also products like Simpleware [66] from Synopsys or Retomo [67] from Beta CAE. Also Matlab has image analysis tools incorporated. However, there is also freeware available. Among the most known ones is Fiji-ImageJ [68] developed at the National Institutes of Health and the Laboratory for Optical and Computational Instrumentation with popular add-ons like Trackmate [69] or Weka [70]. At the European Synchrotron Radiation Facility (ESRF) and the Grenoble Alps University, the Python package Spam [71] has been developed to analyse three-dimensional data-sets with a focus on mechanical analysis. Especially this holistic point of view, creating an image analysis in a way that further analyses, e.g., mechanical numerical simulations, can easily be performed, is central for high quality studies.

For fibre reinforced composites the morphologies of interest are often voids or fibre volume fraction. Mortensen et al. [72] for example investigated the influence of the fibre volume fraction on the fatigue performance of non-crimp fabric reinforced composites. However, in most cases the structure of the composite, the fibre orientations, are in the focus of image analysis of fibre reinforced composites. There are two main approaches available. One is a single fibre tracking analysis, the other estimates the fibre orientations based on the gradients of the grey-scale values. Fibre tracking algorithms are included in some of the above mentioned commercial software as Avizo or Retomo, but can also be carried out with the Fiji-ImageJ add-on Weka or the supervised image analysis method Insegt [73, 74], equipped with a Matlab-based graphical user interface. The fibre tracking methods differ in the approaches they take and in the amount of parameters that need to be set. All of them, however, have in common that they require high-resolution images characterised by little noise to function accurately. The other option is so-called structure tensor methods [64, 75, 76, 77]. As these do not track single fibres but compute a dominant material orientation they are not restricted to fibre analysis. Further, they are less prone to noise and can even handle lower resolutions than fibre tracking methods. The code of Jeppesen et al. [64] is open access and available as Python package [78]. With $\nabla V = [V_{,x}\ V_{,y}\ V_{,z}]^T$ as gradient of the voxel grey-scale values V the structure tensor $\boldsymbol{S}$ is computed as

$$\boldsymbol{S} = \sum \nabla V (\nabla V)^T. \tag{1.3}$$

The summation in Equation 1.3 is defined in a certain domain around the regarded point. The equation can be modified by applying a Gaussian window for the integration. With an additional Gaussian derivative for the gradient computation, Equation 1.4 is obtained. Since voxels have only one grey-scale value, computing a gradient of discrete values is not straight-forward. The gradient needs to be approximated. Due to noise in the image data it is beneficial to apply a filter, as noise is enhanced in differentiation. Smoothing (Gaussian filter) and gradient computation (Central difference scheme) are

combined to a Gaussian derivative which is computationally more efficient. The so-called noise scale parameter σ indicates a domain size that is filtered for the gradient computation ∇V_σ. The so-called integration scale parameter ρ, on the other hand, characterises the standard deviation of the Gaussian kernel K_ρ. In other words, ρ defines the dimension in which the material orientation is analysed.

$$\boldsymbol{S} = K_\rho(\nabla V_\sigma(\nabla V_\sigma)^T) \tag{1.4}$$

An eigendecomposition of $\boldsymbol{S}$ delivers the predominant material orientations. With its properties as symmetric and positive semi-definite tensor, three orthogonal eigenvectors accompanied by three positive eigenvalues are obtained. The smallest eigenvalue with its corresponding eigenvector indicates the fibre direction.

1.4 Image-based modelling

For the preponderant part of acquired image data-sets the analysis is stopped at the image analysis stage, even though image-based modelling adds significant value to imaging. There are two main reasons for this. Firstly, image-based modelling does not simplify the modelling process but adds complexity. One needs to target the modelling towards the image data and understand the issues and uncertainties that come with imaging [79]. Secondly, different research fields need to work together and find a common scientific language, which is, in many cases, challenging. Nevertheless, remarkable studies have been published in recent years.

Wilhelmsson et al. [80] used X-ray computed tomography data to numerically predict compressive failure in unidirectional carbon fibre reinforced composites with off-axis angles up to 20°. In another study a multi-scale modelling approach is taken to predict the damage and fracture behaviour of carbon fibre reinforced composites based on X-ray computed tomography scans [81]. Therefore, micro-scale models with single fibres are created based on high-resolution scans. These are then used to simulate the material response on a ply-level for a tensile test to failure.

When modelling fibre fabric composites there are two options available. One is a direct voxel-based meshing approach. This is usually very easy to implement and can be automated [82, 83]. It raises, however, the research question how to handle voxels which cover two phases, e.g., fibre bundles and resin-rich areas [84]. In addition, the jagged bundle surface introduces unrealistic stress concentrations [85]. The other method is a geometrical representation of the fibre bundles [86]. This process is significantly more complex and time-consuming. Ewert et al. [87] compared the mechanical stiffness response for a three-dimensional woven composite for the voxel-based and geometrical representation methods. Even though the given issues with the voxel-based approach, mesh type and size, accurate local fibre volume fraction, and orientation show a greater influence than the chosen bundle segmentation approach.

Usually, image-based numerical models use the finite element approach, but Fast-Fourier-Transform solutions offer advantages [88]. Those methods are cheap regarding required memory, which is in particular suitable for large three-dimensional image data with several hundred million or even billion voxels. In Kabel et al. [89] an approach is

presented on how to use Fast-Fourier-Transform solvers and more specifically Lippmann-Schwinger solvers on a voxel-based mesh. Here, voxels which contain two phases, e.g., fibre and matrix, are homogenised following mixing rules.

Image-based modelling can be helpful to create models for all fibrous composites, but especially for natural fibre composites. The above mentioned drawbacks of natural fibre composites require for further characterisation during development [90]. Straumit et al. [91] have presented a finite element method to calculate the modulus of flax fibres based on quasi unidirectional flax fibre composite. Here, the fibre misalignments are incorporated via the analysis of three-dimensional X-ray images.

1.5   Research objectives

Within the time frame of this research project, great progress in all different fields of tomography has been accomplished. This active research indicates the enormous possibilities tomography offers and the important role it will play in the future. However, often focus is only on one specific domain of tomography, as the full image-based modelling process from acquisition, reconstruction, segmentation and modelling requires research input from different fields. It can be difficult to organise a research team and find a common scientific language. Albeit the described challenges, the main goal of this research project has been to define a clear process for X-ray computed tomography-based modelling that includes all steps. As for all chains, it also applies for image-based modelling; the weakest link defines the strength of the analysis. The second goal has been to show in different studies the progress in material modelling of fibrous composites that can be achieved if special attention is paid to the importance of a holistic point of view on image-based modelling.

X-ray computed tomography aided engineering - XAE

In this chapter the X-ray computed tomography aided engineering process, initially proposed in Paper A, that defines the framework for image-based modelling, is presented. This process is designed to facilitate and optimise modelling based on X-ray computed tomography imaging.

Despite the progress in image analysis, the analysis of X-ray computed tomography data remains incomplete without image-based modelling. By utilising image-based modelling, the material behaviour of an actual part can be numerically predicted. However, image-based modelling is a complex and time-consuming process, and requires new approaches to extract the maximum information from the image data. The right imaging technology must be chosen, the best scanning settings be found, a suitable reconstruction algorithm be applied, a tailored image analysis be implemented, and a smart way of meshing and homogenising be set up. All with the single purpose to be in line with the modelling and discretisation approach for the material behaviour to be predicted. In other words, the modelling goal must be defined first and the other work steps must be chosen accordingly. In addition, these decisions must be taken with respect to the material properties of the sample to be scanned.

However, only by taking a holistic perspective and targeting all the steps involved in an X-ray computed tomography analysis towards the final modelling goal, the maximum benefit from image-based modelling can be derived. Therefore, the term 'X-ray computed tomography aided engineering' (Figure 2.1) has been coined to emphasise the importance of this comprehensive approach. The naming XAE is deliberately close to Computer-aided

engineering (CAE), but it has neither the intention nor the chance to replace it. It can be rather seen as a tool that allows for a more accurate material behaviour reflection.

Sample	Image acquisition	Image analysis	Meshing	Mapping	Material model	Numerical results

Figure 2.1: *The originally proposed X-ray computed tomography aided engineering (XAE) process with a holistic perspective [61]. All work steps must be in line with the final modelling goal.*

2.1 Imaging

The original focus has been on micro computed tomography, but also the potentials of small angle X-ray scattering tensor tomography have been studied for image-based modelling. Small angle X-ray scattering tensor tomography offers the advantage that it can directly output a material orientation. As it is often the fibre orientation in fibre reinforced composites that is of interest in image-based modelling , the image analysis can be circumvented and the process simplified. In Table 2.1 the applied imaging technologies for the studied material systems are compared for each study.

Table 2.1: Overview of the scanned material systems and the applied imaging technologies.

	Paper A & B	**Paper C**	**Paper D**	**Paper E**
Imaging type	μX-ray computed tomography	μX-ray computed tomography	Helical μX-ray computed tomography	Small angle X-ray scattering tensor tomography
Material type	Non-crimp fabric glass fibre reinforced polymer	Non-crimp fabric glass fibre reinforced polymer	Injection moulded short glass fibre reinforced polymer	Extruded short carbon fibre reinforced polymer

2.1.1 Micro X-ray computed tomography

The scans for **Paper A–C** have been acquired on a standard micro X-ray computed tomography system at the Technical University of Denmark (DTU) in Denmark. Here, conventional voxel-sizes of 5 µm - 11 µm for resolving glass fibres with a diameter of approximately 20 µm have been used. Those comparatively high resolutions lead at the same time to long acquisition times and large data sizes, which pose a more challenging image analysis. In **Paper D** on the other hand the low resolution with a voxel-size of 60 µm has been used, resulting in a much larger field of view and shorter scan times as well as a smaller data size. This scan has been acquired on a helical scanning set-up at the Henry Moseley X-ray Imaging Facility, UK, which is ideal for slender samples as the vertical stitching of several scans is omitted. In Table 2.2 some of the imaging parameters are listed.

Table 2.2: Overview of different scanning parameters in **Paper A–D**.

	Paper A & B	Paper C	Paper D
Scanner	Zeiss Xradia Versa 520	Zeiss Xradia Versa 520	Thermo Fisher Scientific Heliscan Mk2
Voxel-size [µm]	5.47 10.9	8	60
No. projections	3601 - 5801	3601	1860
Scan times [h]	21 - 72	72	0.5
Data sizes [GB]	1.7 - 13.5	9.7	3.5
Field of view [mm^3]	$4.2 \times 11 \times 23$	$4.7 \times 15 \times 34$	$29 \times 67 \times 204$

2.1.2 Small angle X-ray scattering tensor tomography

The Small angle X-ray scattering tensor tomography scans have been acquired at the Swiss Light Source X-ray beamline Tomcat at the Paul Scherer Institut (PSI) in Switzerland. Between the sample and the detector, a circular grating with a fine period $g = 1.46\,\mu m$ and a coarse period $P = 49.5\,\mu m$ was placed. The sample was mounted on a 2-axis stage. Additionally to the rotation the sample can thereby be tilted by $\pm 45°$ as well. In total, 1000 projections with an exposure time of 10 ms per image tile have been acquired. The 1000 projections assemble of 100 rotation angles $[0°, 3.6°, \ldots, 356.4°]$ at 10 tilt angles $[0°, 5°, \ldots, 45°]$. For 21 single image tiles, the effective scanning time was approximately 210 s, which is added to the 210 s required for the sample stage movements. For the voxel-size of 100 µm, the stitched field of view is $38.2 \times 38.2 \times 28.6$ mm^3.

The reconstruction of the projection images does not yield a unique grey-scale value for each voxel but a unique second-order scattering tensor per voxel. The eigenvector with the smallest eigenvalue can be interpreted as the dominant material orientation. In case all three eigenvalues of the second order scattering tensor are equally large, a random fibre orientation is evident within the respective voxel. In the case where one eigenvalue is approaching zero, perfect fibre alignment within this voxel can be assumed.

2.2 Image analysis

In **Paper A–C** non-crimp fabric reinforced glass fibre composites have been analysed. The defined bundle structure of the fabrics allowed the image analysis to be divided into in two different parts. One is a surface segmentation, where the surface of fibre bundles has been segmented against resin-rich areas. This has been achieved both by thresholding the different grey-scale values of fibre bundles and resin-rich areas, and single bundle detection. The single fibre bundle detection presented in **Paper C** is capable of segmenting fibre bundles individually, even though these are in contact with each other over larger areas. For this purpose the image intensities are radially sampled along a centre line. The segmentation task is then regarded as a binary optimisation following Li et al. [92], extended by a penetration check [93]. An interface between fibre bundles and resin-rich areas, included in the finite element model, is advantageous to unveil stress concentrations compared to a regular voxel-based mesh. However, the surface
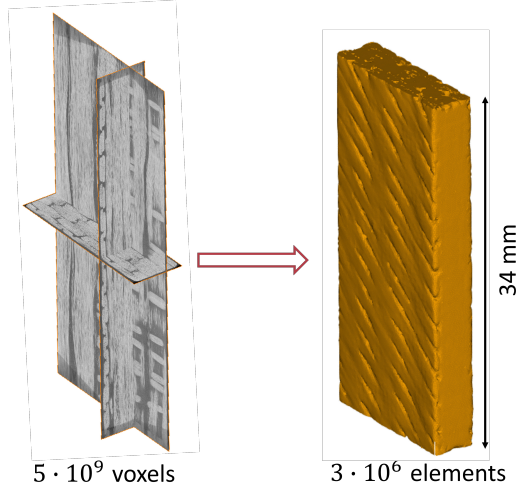
5 · 10⁹ voxels   3 · 10⁶ elements

Figure 2.2: *Down-scaling of image data richness to a finite element mesh from **Paper C**. Here, a down-scaling factor of three orders of magnitudes is not uncommon. This down-scaling process naturally comes with issues and compromises must be made.*

segmentation of fibre bundles is much more complex. The reason for this complexity lies in the scale difference between voxel-size and element size. In **Paper C**, for example, the image data consisted of $596 \times 1922 \times 4228 = 5,019,616,896$ voxels. To handle 5 billion elements is unrealistic and indeed not necessary. The final finite element model comprises, depending on the mesh size and type, between 0.5 and 2.9 million elements (Figure 2.2). To reach these more realistic numbers the very detailed segmented surface, based on element lengths close to the voxel-size, must be smoothed. This smoothing process is particularly time consuming for a thresholding-based surface mesh. It can last up to a full working day to generate the final mesh for image data-sets of the type presented in **Paper A–C**. Therefore, the above-mentioned single bundle segmentation method should be chosen, but more research is necessary to fully automate the process.

The subsequent phase of the image analysis focused on analysing the orientation of the fibres. In **Paper A** and **Paper B** a fibre tracing method in Avizo has been applied. Here, single fibres are detected and then traced through the volume. This is computationally heavy and can take up to six hours depending on the available computational power and the chosen tracking parameters. In contrast, the structure tensor method, used in **Paper C**, does not track individual fibres but computes a predominant material orientation, which is computationally more efficient in terms of required hardware, software, and computation time. By implementing the open-source structure tensor method, the computation can be performed on a standard 32 Gigabyte central processing unit in approximately 20 minutes. This presents a significant advantage compared to fibre tracking using commercial software packages and the associated workstation requirements as in **Paper A** and **Paper B** (Central processing unit 256 Gigabyte and graphic processing unit 12 Gigabyte).

For **Paper D** the same structure tensor code as in **Paper C** has been used to analyse
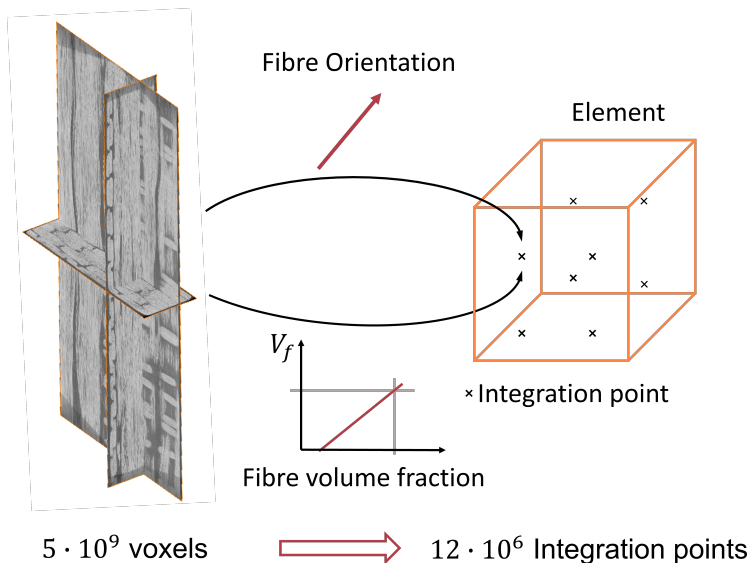
Figure 2.3: *Visualisation of a typical mapping process for fibrous composite models. Often fibre orientation and fibre volume fraction are mapped either element-wise or integration point-wise. Also here, a drastic down-scaling of data richness is involved. The voxel and integration point numbers are taken as an example from* **Paper C**.

an injection moulded glass fibre reinforced polymer. The strength of the structure tensor method to estimate fibre orientations with voxel-sizes significantly larger than the fibre diameter has been exploited in this study. For high-resolution scans the two parameters that need to be defined for the structure tensor code show a low sensitivity to changes. However, for the chosen low resolution of a voxel-size $60\,\mu\text{m}$, corresponding to three times the fibre diameter, the parameters must be chosen carefully as low-resolution scans tend to incorporate higher noise levels.

As the reconstruction of the image data in **Paper E** directly computes a fibre orientation, no image analysis has been required in this study.

2.3   Mapping

The mapping process is a key element in the whole XAE process. It may not require the most computation or development time, but it represents the intersection where the imaging and modelling parts need to meet. Given the large voxel numbers of regular image data-sets, a direct transfer of image data to the numerical model is not feasible. Thus, the image data need to be compressed during its mapping onto the numerical model (Figure 2.3). The challenge here is to decide how to compress or to homogenise the image data and which data to neglect. There is no general solution to this problem but in each process it must be decided individually on how to approach this challenge.

Table 2.3: Overview of different mapping schemes that have been developed for **Paper A–E**.

	Paper A & B	**Paper C**	**Paper D**	**Paper E**
Element types	Irregular tetrahedrons	Irregular tetrahedrons & hexahedrons	Irregular shells	Regular hexahedrons
Target	Elements	Elements & Integration points	Integration Points	Integration Points
Mapped entity	Fibre orientations	Material orientations	Material orientations	Rotated stiffness matrix
Homogenisation	-	-	x	-

The importance of this research question is stressed with **Paper F**.

Applied to fibre reinforced composites, the amount of voxels which carry a material orientation or even tracked fibres is regularly much higher than the amount of mapping targets, e.g., elements or integration points. In **Paper E** for example, the amount of voxels is 64 times higher than the amount of integration points, in **Paper D** this factor is even 4,200. The question therefore is how to condense the rich image information into the finite element model. One natural homogenisation approach would be to calculate the mean orientation of all voxels represented by one integration point. However, calculating a mean will inevitably lead to smeared orientations. Fibre orientation outliers, e.g., large misalignments, will never be implemented in the finite element model. Such fibre misalignments have proven to be critical for strength analyses [94].

These considerations underline the significance of the holistic perspective in XAE. Also, the mapping algorithm need to be in line with the modelling goal. Thus, different mapping schemes have been developed (Table 2.3) for the different studies. The target element types are various: Regular and irregular, first and second order, two-dimensional and three-dimensional elements. Both element-wise and integration point-wise mapping schemes have been presented. In **Paper A** and **Paper B** the fibre orientations from the tracked fibres are mapped element-wise. For the mapping scheme in **Paper C**, described in **Paper F**, an external file with the integration point coordinates must be read in. This detour has been removed in **Paper D** and **Paper E**, where the integration points are directly computed in the code based on the node/element formulation. Figure 2.4 visualises the computed integration points for an irregular shell mesh. With the used structure tensor method in **Paper C** and **Paper D** no individual fibres but a dominant material orientation is mapped. In **Paper E** a special modelling approach (described in the next section) has been developed which is necessary due to the large voxel-size of 100 µm compared to the carbon fibre diameter of approximately 7 µm. Therefore, the order Mapping - Modelling is changed and the stiffness tensor is computed first and then mapped integration point-wise.
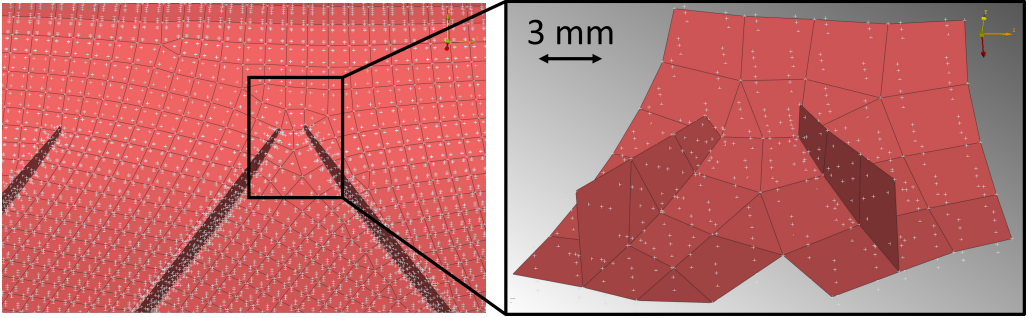
Figure 2.4: *Computed integration points (grey crosses), which represent the mapping target in **Paper D**, for the two-dimensional shell mesh. Quadrilateral elements have four integration points per element, while triangular elements have only one. In total, there are five integration point layers per element.*

2.4 Modelling

Since image-based modelling of fibrous composites is a new research field, focus has been on accurate prediction of the most important material parameter, the elastic tensile modulus. As the fibre orientation is strongly linked to the elastic modulus, the fibre orientation analysis is an important part of the studies. Thereby, a good match between experimentally and numerically determined elastic moduli is an indicator for an accurate fibre orientation analysis. For **Paper A**–**C** a linear orthotrophic material model has been assigned for the fibre bundles. In **Paper A** and **Paper B** the required nine independent material parameters have been calculated based on homogenisation with the periodic boundary model EasyPBC [95]. The fibre and matrix stiffness as well as the Poisson´s ratios must be given as input. Additionally, the fibre volume fraction is included via the fibre radius in this single fibre representative volume model. In **Paper C** these nine material parameters have been calculated by the micro-mechanics model of Chamis [96]. The differences in the results between EasyPBC and Chamis are small in the studied case.

In **Paper D** material modelling has not been part of the study, while in **Paper E** a more advanced material model is presented. Here, the low-resolution imaging requires a novel way to create the material's constitutive law. This has been set up within a framework to account for a composite with anisotropic short fibres. For this framework the model by Mori-Tanaka [97] has been implemented. Therefore, a strain localisation tensor must be calculated. It is defined according to Benveniste et al. [98, 99], based on the Eshelby tensor [100]. The Eshelby tensor is formulated on the theory that the strain for an ellipsoidal and homogeneous inclusion within an infinite matrix is constant. It is expressed as

$$\boldsymbol{A}^{MT} = \left[\boldsymbol{I} + \boldsymbol{P} : \left((\boldsymbol{C^m})^{-1} : \boldsymbol{C^f} - \boldsymbol{I} \right) \right]^{-1} \tag{2.1}$$

and incorporates the identity tensor $\boldsymbol{I}$, the matrix $\boldsymbol{C^m}$ and fibre $\boldsymbol{C^f}$ stiffness tensors, and Eshelby's tensor $\boldsymbol{P}$, which solely depends on the inclusion geometry and the matrix Poisson's ratio.

Finally, the fourth order Mori-Tanaka stiffness tensor $\boldsymbol{C^{MT}}$ depends on $\boldsymbol{I}$, $\boldsymbol{C^m}$, $\boldsymbol{C^f}$ as well as the scalar value of the fibre volume fraction V_f.

$$\boldsymbol{C^{MT}} = \boldsymbol{C^m} + V_f \left(\boldsymbol{C^f} - \boldsymbol{C^m} \right) : \boldsymbol{A^{MT}} \left[(1 - V_f)\boldsymbol{I} + V_f \boldsymbol{A^{MT}} \right]^{-1} \tag{2.2}$$

To account for different fibre orientation vectors $\boldsymbol{p}$ the stiffness tensor must be rotated accordingly. The fibre orientations are obtained from the second order scattering tensor. Here, the eigenvector with the smallest eigenvalue defines the dominant material orientation. For the chosen voxel size of $100\,\mu m$ and a fibre diameter of approximately $7\,\mu m$ it must be assumed that there are several fibres present within one voxel. Therefore, extra care must be taken in setting up the material model, as explained with the following imaginary case.

(a) (b)
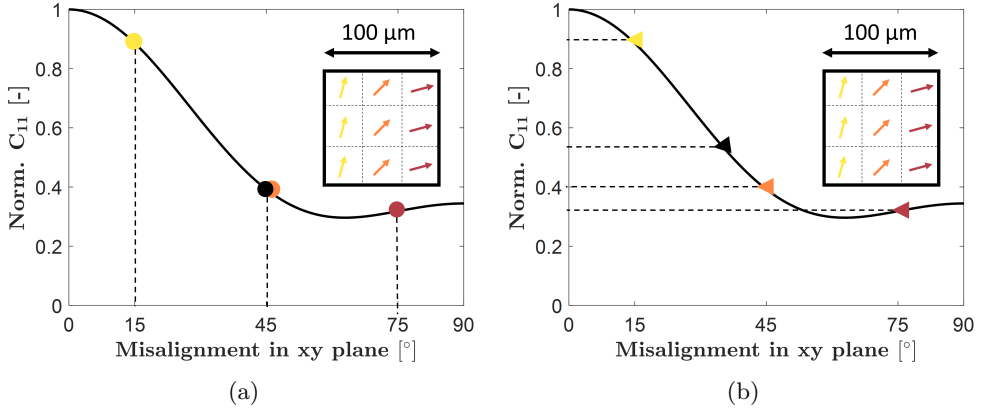
Figure 2.5: *Visualisation from **Paper E** of the influence of the non-linear relation between fibre orientation and mechanical stiffness properties. (a) In case there are three different fibre orientation regimes with $15°$, $45°$ and $75°$ within one voxel with a size of $100\,\mu m$ the mean fibre orientation is $45°$, indicated by the black dot. (b) The mean of the stiffness matrix components C_{11}, indicated by the black triangle, however, does not coincide with the mean orientation due to the non-linear correlation between fibre orientation and stiffness property.*

With three fibres each, oriented at $15°$, $45°$ and $75°$ within one voxel, the mean orientation is $45°$ (Figure 2.5a). If on the other hand, the mean of the stiffness matrix components, C_{11} in this case, is considered (Figure 2.5b), it differs from the mean of the fibre orientations due to the non-linear relation between fibre orientation and stiffness matrix components. Therefore, the chosen voxel-size is too large for accurate modelling. The fibres should be resolved individually and then homogenised.

However, the scattering tensor does not only deliver the dominant fibre orientation in form of the eigenvector with the lowest eigenvalue, it also delivers two other eigenvalues. The remaining two eigenvalues of the scattering tensor represent the fibre orientation distribution, or in other words, how well the fibres are aligned within one voxel. The

new term, Directional Anisotropy, has been introduced to account for this sub-voxel fibre orientation spread. It is given in xy and xz-plane in Equations 2.3 and 2.4, where λ_i represents the eigenvalues.

$$DA_{xy} = \frac{\lambda_3}{\lambda_1} \tag{2.3}$$

$$DA_{xz} = \frac{\lambda_3}{\lambda_2} \tag{2.4}$$
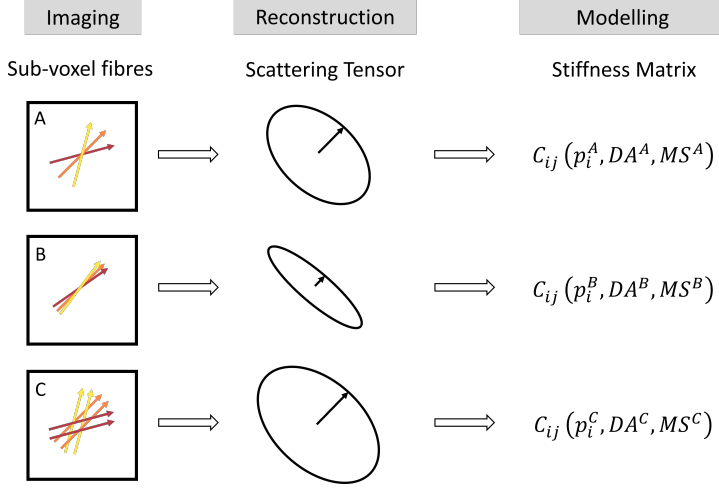
Figure 2.6: *Visualisation from **Paper E** of three voxels with different sub-voxel fibre orientation distribution and fibre volume fraction. All voxels show the same dominant fibre orientation, but yield different ellipsoid shapes representing the X-ray scattering tensor. These different shapes are used to construct different stiffness matrices C_{ij} (Equation 2.6). Consequently, the stiffness matrix depends on the dominant fibre orientation p_i, the Directional Anisotropy (DA) (Equation 2.3, 2.4) and the Mean Scattering (MS) used in Equation 2.5.*

A ratio of 1 signifies a fully random orientation, while a ratio of 0 represents perfect alignment. This ratio is set in a linear relation to the sub-voxel fibre orientation spread. With this sub-voxel fibre orientation spread, an update for each stiffness matrix component is computed. Additionally, the scattering tensor information is used to include a local fibre volume fraction, linearly depending on the local mean scattering MS^{local} of each voxel. It is expressed as

$$V_f^{local} = -\frac{V_f^{mean}}{MS_c - MS_m} MS_m + \frac{V_f^{mean}}{MS_c - MS_m} MS^{local}, \tag{2.5}$$

where MS_m represents the mean scattering of the pure matirx, while the mean scattering of all voxels MS_c corresponds to the mean fibre volume fraction V_f^{mean}. Thereby, for

each integration point a separate stiffness matrix, including the sub-voxel fibre orientation spread and the local fibre volume fraction, is computed (Figure 2.5c) and mapped.

On the basis of the Mori-Tanaka framework the stiffness tensor can then be expressed in Voigt form as a function of the fibre orientation p_i, the Mean Scattering (MS) and the Directional Anisotropy (DA) as following,

$$C_{ij} = C_{ij}\left(p_i, DA, MS\right). \tag{2.6}$$

The new way to set up the stiffness matrix is visualised in Figure 2.6. The voxels in the figure all show the same mean fibre orientation. However, voxel A and B have a different distribution and hence, a different Directional Anisotropy (DA). Voxel A and C on the other hand exhibit the same distribution but Voxel C has a higher fibre volume fraction and hence, they are characterised by a different Mean Scattering (MS).

Results

This chapter presents the main achievements of the research projects reported in this thesis. In particular, the results of low-resolution scans as well as different load cases for different materials and imaging technologies are discussed.

Paper A laid the groundwork for all following papers, where we proposed the holistic image-based modelling concept XAE, which has been key for all studies. It is showcased for a non-crimp fabric glass fibre reinforced composite, where the bundle structure was geometrically segmented from resin-rich areas. Additionally, a fibre tracking analysis scheme has been used to map fibre orientations element-wise. This allows to accurately predict the tensile modulus of the scanned samples (Table 3.1).

Paper B is directly based on **Paper A** and presents a more detailed analysis of stress concentrations in the studied composite for different image analysis methods. In tension-tension fatigue investigations of composites with similar layups and mechanical properties, it has been shown that intersections of unidirectional bundles and off-axis backing bundles are one of the main drivers of fibre failure [14, 15]. Those intersections are the same areas that showed the highest stresses in the image-based model in **Paper B**. It is worth noting that the scan has been taken in an unloaded state and the model simulated a static tensile loading. One of the presented image analysis methods allows to remove the backing bundles from the model. Even in this case the stress concentrations in the unidirectional bundles remain. This is a clear indicator that at least partly the fibre failure under fatigue loading is caused by the waviness of the unidirectional bundles. Further evidence of the stress states causing fibre failure remains for future research.

Table 3.1: Results of the tensile modulus results, measured along the dominant fibre orientation, in **Paper A** comparing the physical tests and the finite element model predictions. The results are normalised with the glass fibre stiffness due to confidentiality reasons. In total eight samples were manufactured; Sample-A, E, G were randomly chosen among them to be scanned.

	Sample-A	Sample-E	Sample-G
Physical test	0.51	0.54	0.52
XAE result	0.51	0.51	0.50
Difference	0.3%	-4.8%	-3.2%

In **Paper C** the image-based modelling of non-crimp fabric glass fibre reinforced composites has been enhanced by the above described structure tensor method and a semi-automated single bundle segmentation procedure. Additionally, the research goal for a field of view enlargement has been defined. It is demonstrated that the implemented structure tensor method is very robust to low-resolution scans. A bisection of the resolution results in a scanning volume increase by a factor of eight. In other words the data size scales cubed with the voxel size change.

3.1 Low-resolution scans

The finite element analysis results developed in **Paper C** are depicted in Figure 3.1 for the four different voxel-sizes. The original data-set with a voxel-size of $8\,\mu m$ has been computationally binned to a voxel-size of $64\,\mu m$, corresponding to a data-size of $9459\,MB$ and $18\,MB$, respectively. Even though thereby 99.8% of the data have been removed, the stress concentrations are still visible. However, the stress distribution appears smeared. This visual impression can be quantified with the stress histograms (Figure 3.1 middle row). The mean value is only reduced by 2.9% from $112\,MPa$ to $109\,MPa$. At the same time the numerically predicted tensile modulus is decreased by 4.7%. The reason for this can be found in the larger voxels which represent more fibres. Such a homogenisation of fibre orientations will always lead from a distinct fibre orientation distribution towards a smeared mean fibre orientation distribution. In the theoretical case of only one voxel for the entire scanned volume, this voxel would represent the mean orientation of all fibres. The obtained small deviations in elastic modulus and mean stress value between high and low-resolution scans can be acceptable in many applications, provided awareness of their existence and severity. In reverse conclusion, it can be dangerous to only rely on low-resolution scans for an unknown material.

Therefore, in **Paper D** the low-resolution X-ray computed tomography of fibrous composites has been further studied and validated by high-resolution scans. This study exploits the low-resolution robustness of the structure tensor method. Additionally, this study illuminates the influence of homogenisation in image analysis and the subsequent

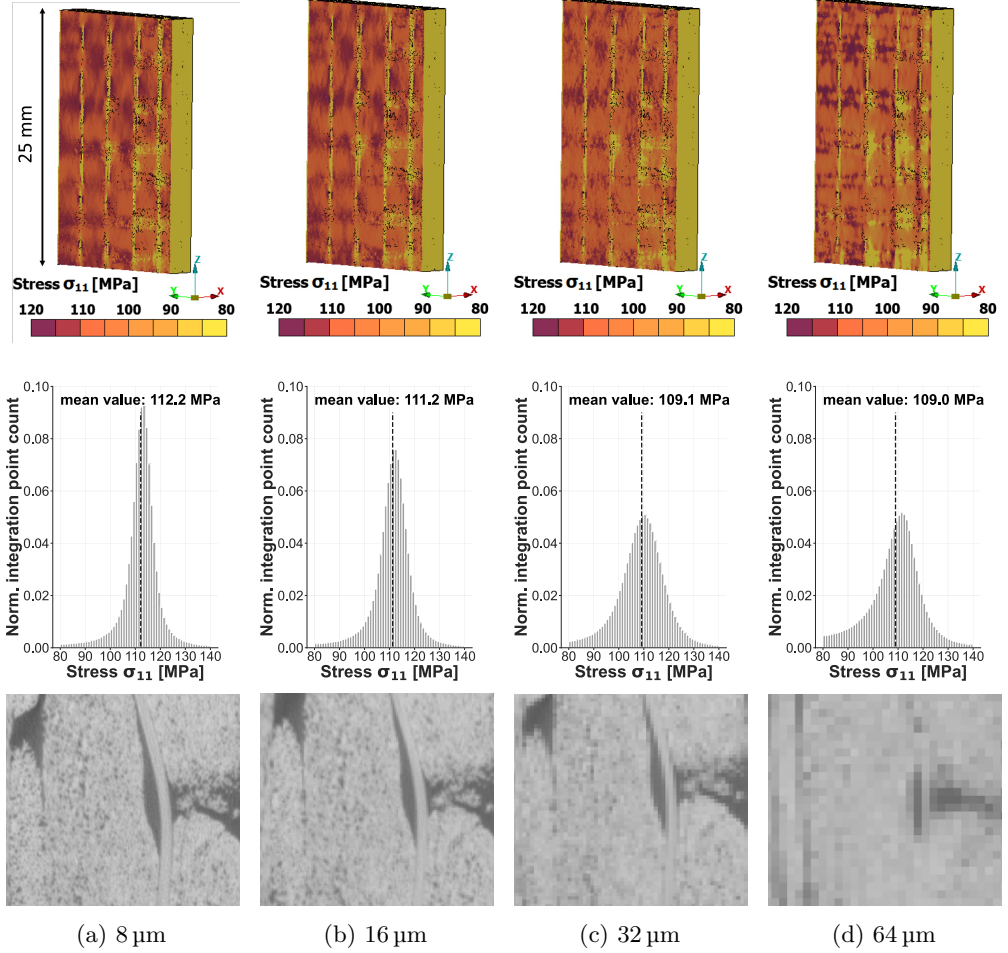Figure 3.1: *Visualisation from **Paper C** of the three-dimensional image resolution influence on the predicted stress distribution in a y-z cross-section at the interface between backing bundles and unidirectional bundles (top row) and the stress distribution in the unidirectional bundles depicted in a histogram (middle row). Examples for the image resolution are shown in the bottom row. [79]*
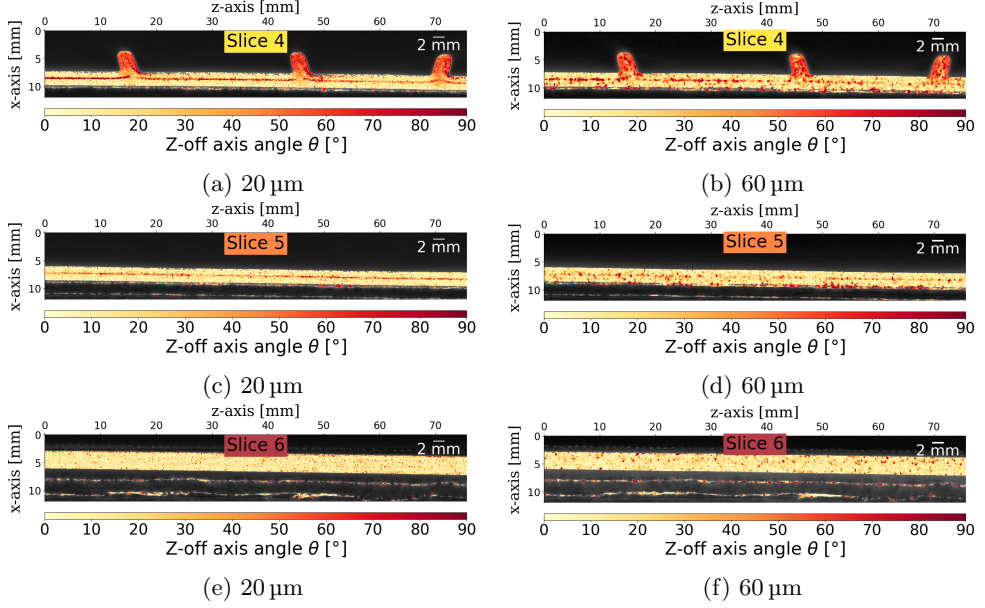
Figure 3.2: *Comparison from **Paper D** of the zenith or z-off axis angle θ mapped onto the original grey-scale images for different cross-sectional slices for the two voxel-sizes 20 µm and 60 µm.*

mapping process. An industrially injection moulded short glass fibre reinforced thermoplastic component with a length of approximately 20 cm has been scanned with a voxel size of 60 µm. In addition, two regions within this component have been scanned with a voxel-size of 20 µm. In Figure 3.2 the zenith angle θ, colour mapped onto the original grey-scale images for three different cross-sectional slices through the image data, is visualised. In general, it can be stated that there is a good match for the two resolutions. The low-resolution scan accurately captures the dominant fibre orientation along the mould flow direction, which approximately coincides with the z-axis. Additionally, the off-axis middle layer, visible in Slice 4 and 5, is detected by the structure tensor analysis in the 60 µm data-set. However, there is always some noise present in an X-ray scan, even more pronounced in a low-resolution scan. This noise is enhanced by the structure tensor method resulting in small regions with off-axis orientation.

This noise enhancement can be reduced by the two available parameters for the structure tensor method. The parameter influence is shown for the integration scale parameter ρ_{ST} in Figure 3.3, as an example. For small values of ρ_{ST} random orientation is estimated. With larger values of the integration scale parameter the noise, which leads to off-axis orientations, is more and more suppressed. Therefore, it is recommended to choose a larger ρ_{ST}. However, for the structure tensor method there is no difference between noise and real fibre misalignments. Therefore, large ρ_{ST} values also suppress local fibre misalignments. In case there are some obstacles in the mould flow which lead to locally different fibre orientations, these would be suppressed as well. Thus, either a

(a) $\sigma_{ST} = 0.5$; $\rho_{ST} = 0.5$

(b) $\sigma_{ST} = 0.5$; $\rho_{ST} = 1.0$

(c) $\sigma_{ST} = 0.5$; $\rho_{ST} = 1.75$

(d) $\sigma_{ST} = 0.5$; $\rho_{ST} = 2.25$
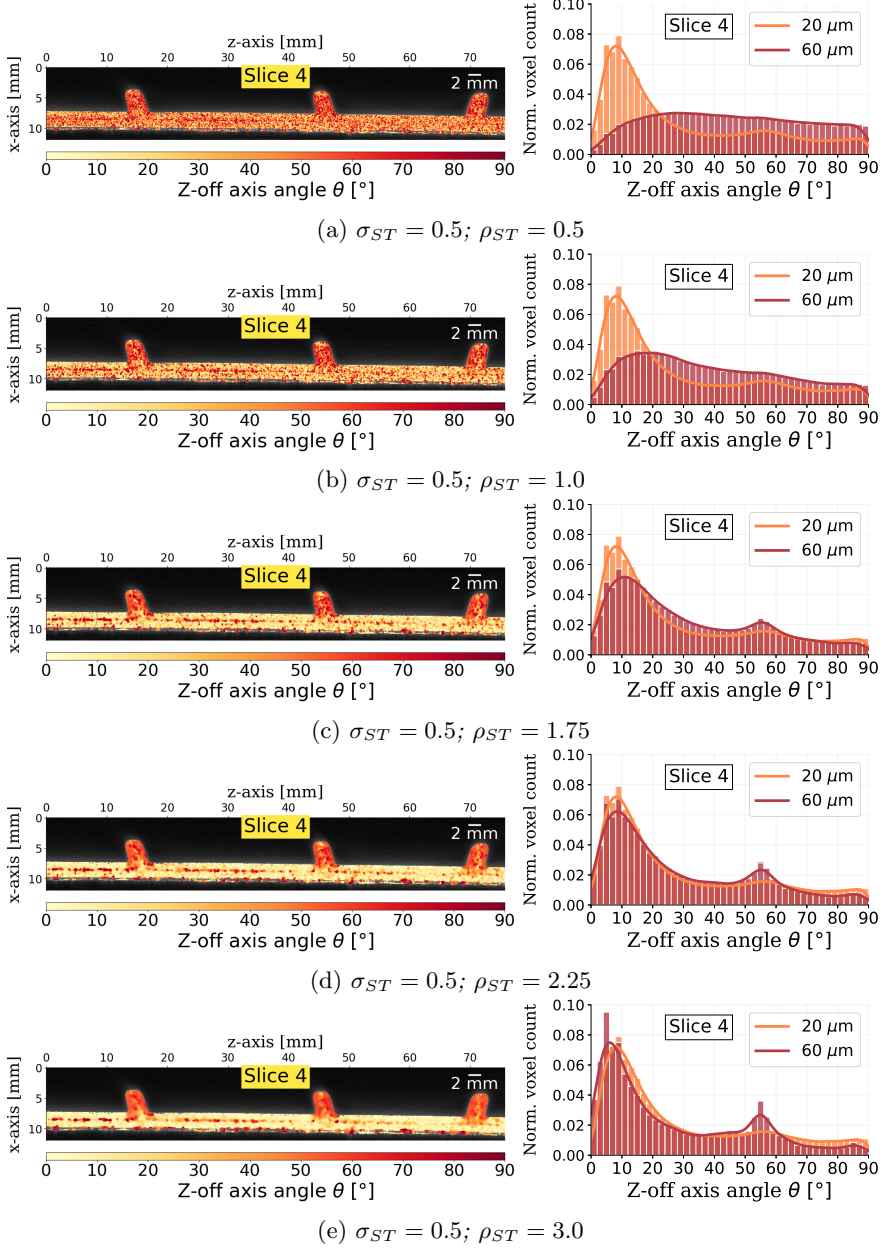

(e) $\sigma_{ST} = 0.5$; $\rho_{ST} = 3.0$

Figure 3.3: *Comparison from* **Paper D** *of the zenith or z-off axis angle θ mapped onto the original grey-scale images (left) and histograms (right) for the same cross-sectional slice for a voxel-size of* 60 μm *for different values of the structure tensor parameter* ρ_{ST}.

compromise for the structure tensor parameters must be found or the parameters must be locally adjusted based on, e.g., fibre orientation change gradients. The latter remains for further research.

The mapping work-step becomes more important the lower the chosen resolution. In case the orientation of each individual fibre is mapped, the mapping process is straightforward. However, for the case presented in **Paper D** with 43,180 target integration points for 207,660,459 source voxels, each with a dominant fibre orientation, the situation is less straightforward. Therefore, a choice must be made on how to transfer orientation information into the target model. There are three possible solutions. One is to compute the mean orientation of all voxels which are associated to each integration point. In the presented case there are approximately 4,200 voxels per integration point. The result is a globally very smooth fibre orientation distribution, local misalignments are just smeared out. Option number two omits any homogenisation during mapping. Thereby, only the fibre orientation of the voxel containing the integration point is mapped. This has proven to give the best representation of the original fibre orientation distribution (see Figure 3.4 and also **Paper E**). However, this approach is prone to induce local noise. The third possibility is an approach somewhere in between option number one and two. In the histograms in Figure 3.5 the results for different homogenisation areas are compared with no homogenisation for the three orientation tensor components a_{ii} (orientation tensors have been first introduced by Advani and Tucker [101]). Here, the mean orientation of 27, 125, 729, and 3375 voxels, respectively, around the target integration point is computed. Especially for the a_{33} component of the second-order orientation tensor (Figure 3.5 right) which represents an orientation along the z-axis, a smearing of the distribution becomes evident for larger homogenisation areas.
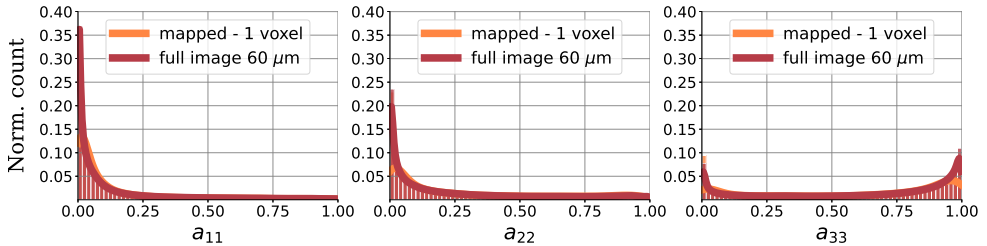
Figure 3.4: *Histograms from* **Paper D** *of the actually mapped and originally computed three a_{ii} components of the second-order orientation tensor based on the three-dimensional image (voxel-size $60\,\mu m$). Both counts are normalised for better comparison. No mapping homogenisation is applied. Only the orientation information of the voxel, the target integration point lies in, is mapped. There are 43,180 target integration points and 207,660,459 source voxels available for mapping.*

The adequate choice of the mapping scheme will always be of high significance and must be adapted from case to case, also with respect to the modelling goal. In particular it must be seen as two-way homogenisation as already the structure tensor method represents a homogenisation. A change in the structure tensor parameters must consequently lead to a change of the mapping homogenisation area.
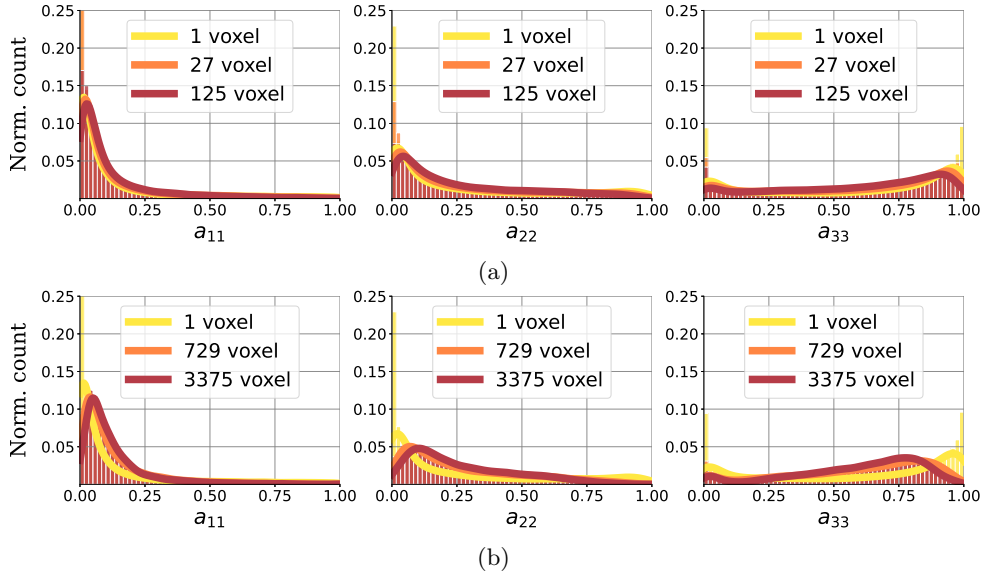
Figure 3.5: *Histograms from **Paper D** of the three a_{ii} components of the mapped second-order orientation tensor for five different homogenisation areas. The fibre orientations are mapped onto 43,180 target integration points. The results for '1 voxel' (yellow curves) does not apply any homogenisation and only uses the the orientation information of the voxel, the target integration point lies in. (a) Three different homogenisation areas where two (orange and red curve) homogenise fibre orientations of 27 and 125 voxels, respectively, around the target integration points. (b) Three different homogenisation areas where two (orange and red curve) homogenise fibre orientations of 729 and 3375 voxels, respectively, around the target integration points.*

3.2   X-ray scattering tensor tomography

Beside the implementation of large-field-of-view X-ray computed tomography scans for industrial applications, also more fundamental imaging research has been performed in **Paper E**. In collaboration with the Swiss Light Source, Paul Scherrer Institute in Switzerland, a novel kind of image-based modelling is presented. The tensor tomography method developed at the synchrotron X-ray beamline TOMCAT is integrated in a holistic XAE approach. The investigated sample is a short carbon fibre reinforced polyether ether ketone composite cylindrical rod with a diameter of 19 mm and a height of 14 mm. As the resolution of the acquired data-set with a voxel-size of 100 μm is very low compared to standard imaging of carbon fibre reinforced composites with voxel-sizes up to 7 μm, special focus has been on how to compensate for low-resolution imaging. The above described modelling approach incorporating the sub-voxel fibre orientation spread and the local fibre volume fraction, both based on the scattering tensor information, enable an accurate prediction of the tensile modulus (Table 3.2). Compared to performing only a standard fibre orientation mapping (Simulation A), the implementation of the sub-voxel

Table 3.2: Comparison from **Paper E** of the experimentally measured tensile modulus and the numerically predicted tensile modulus of the three simulation variants. *Simulation A* uses the dominant fibre orientation and a global fibre volume fraction of 19.9 %. *Simulation B* incorporates sub-voxel fibre orientation information from the scattering tensor and a global fibre volume fraction of 19.9 %. In *Simulation C*, additionally to the sub-voxel fibre orientation information, a sub-voxel fibre volume fraction is assigned.

	Simulation A	Simulation B	Simulation C	Experiment
Sub-voxel fibre orientation	-	x	x	
Sub-voxel fibre volume fraction	-	-	x	
Tensile Modulus [GPa]	8.2	8.6	9.1	9.22 ± 0.044
Deviation from Experiment	$-11.6\,\%$	$-6.5\,\%$	$-1.6\,\%$	

fibre orientation information (Simulation B) and additionally of the local fibre volume fraction (Simulation C) lead to a significant improvement. The tensile modulus is only underestimated by $-1.6\,\%$ in Simulation C in contrast to $-11.6\,\%$ for Simulation A. Thus, it has been shown that even such low resolutions with voxel-sizes approximately fifteen times the fibre diameter allow for accurate tensile modulus prediction given an advanced imaging technology and targeted modelling approach is used. With the approach presented in **Paper E** volumetric scanning field of views for carbon fibre reinforced composites can be increased by three to six orders of magnitude. These results mark a tremendous step forward towards large field of view analyses of fibre reinforced composites.

In addition to the tensile modulus, also the axial stress distribution inside the sample and the axial stress histogram are studied (Figure 3.6). The influence of the sub-voxel fibre orientation information is not very distinct (Figure 3.6a and b). Stress concentrations in Simulation A appear more smeared in Simulation B, as with the orientation update fibre orientations are smeared and hence high stresses reduced. In Figure 3.6c the influence of the local fibre volume fraction update becomes apparent. The mean scattering signal has been particularly high in the core of the sample and in the extreme periphery. A high scattering signal signifies a high fibre content in the reconstructed voxel. Consequently, also high stress is predicted in the numerical model. The differences in the stress histogram (Figure 3.6d) are more difficult to capture. An important effect to mention is that the peak of the stresses for Simulation C is lower but shifted to higher values at the same time. For Simulation A and B there is a maximal possible stress value which is reached when the fibres are aligned in axial direction. For Simulation C in addition the local fibre volume fraction must be high in these integration points.

(a) *Simulation A*   (b) *Simulation B*   (c) *Simulation C*

(d) *Histogram stresses σ_{xx} Simulation A–C*
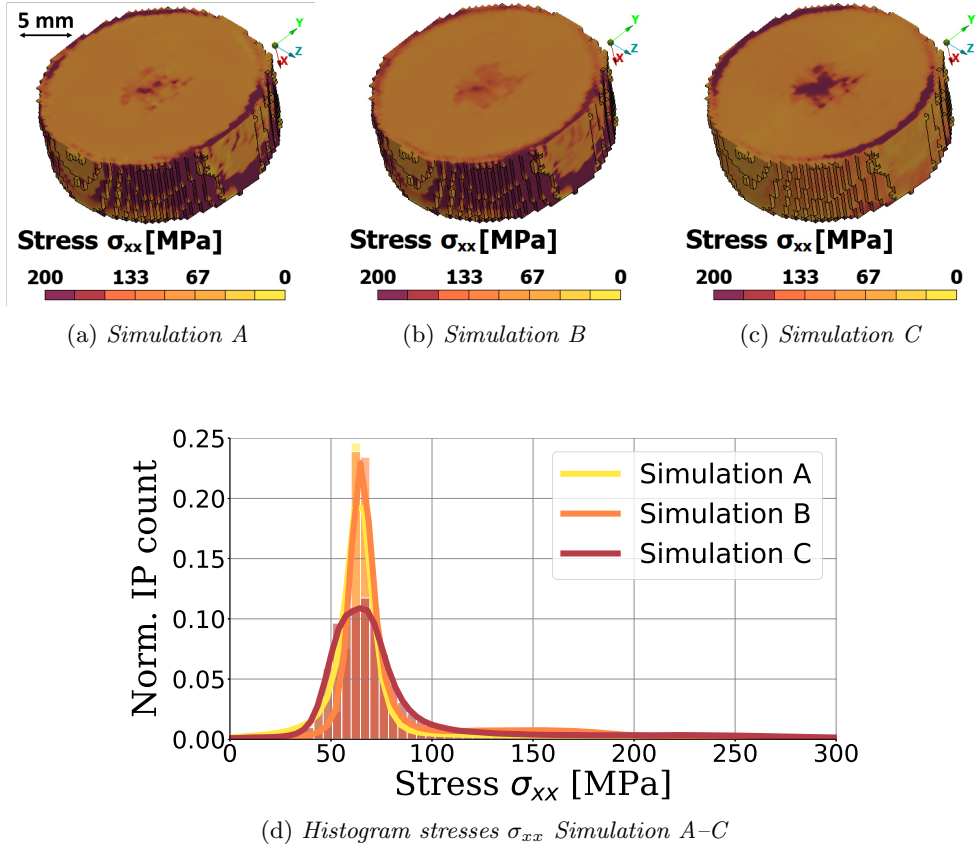
Figure 3.6: *Comparison from **Paper E** of stresses in axial direction for all three simulation variants. Simulation A uses the dominant fibre orientation and a global fibre volume fraction of 19.9%. Simulation B incorporates sub-voxel fibre orientation information from the scattering tensor and a global fibre volume fraction of 19.9%. In Simulation C, additionally to the sub-voxel fibre orientation information, a sub-voxel fibre volume fraction is assigned.*

CHAPTER 4

Future research

Future research options are vast. The progress in imaging research is fast, much faster than in image-based modelling. Phase-contrast scanning and small angle X-ray scattering tensor tomography used to be limited to synchrotron facilities, but they are becoming available on lab-based systems and have been tested within this project. Both imaging technologies show promising capabilities to address two major issues in X-ray computed tomography; low contrast between fibres and matrix for organic fibre reinforced composites, and limited fields of view.

Further, with the new *MAX IV* synchrotron of fourth generation, in Lund, Sweden, exciting new possibilities are arising, especially for Swedish and Danish material research teams. Many beamlines at this facility allow for multi-modal imaging, facilitating a swift change between, e.g., small angle X-ray scattering to micro computed tomography. Consequently, the material's structure and morphology can easily be studied during one beamtime.

Reconstruction and image analysis are classical mathematics dominated research areas, which have recently seen high popularity. Constantly new methods are introduced. Lately, machine learning combined with classical approaches in the respected fields has become popular. But this can change swiftly with the advent of new methods and increased computational power.

Even though reconstruction is the very basis for tomography, no special focus has been on investigating the influence of different reconstruction schemes and parameters within this project. More research is needed to align reconstruction algorithms with the

modelling goal to optimise the quality of the entire image-based modelling process.

However, with manifold options for acquisition, reconstruction and image analysis it can become challenging from a material modelling perspective to keep up with all advances and choose the right approach for a certain material analysis goal. More exchange between the imaging and modelling research areas is necessary to advance in quality and not only in quantity of produced scans and image-based models.

Strength of heterogeneous, brittle, materials is controlled by the largest defect, e.g., fibre misalignment. The methods presented here have so far only been validated with respect to elastic modulus, which, in contrast, to strength is controlled by the average fibre orientation and not by the maximum misalignment angle. Consequently, it remains to assess the proposed XAE method for its ability to predict strength, and to make potentially required adaptions to the model for identification and analyses of critical defects.

CHAPTER 5

Concluding remarks

Image-based material modelling from nanometre to metre scale will become a standard in numerical modelling

X-ray computed tomography three-dimensional image-based modelling is a rather young research field. First studies were published around ten years ago and it has since seen enormous progress. The performance of the underlying image analysis is constantly improving, which allows for new modelling approaches. On the other hand there are plenty of sophisticated methods in composite mechanics available that can greatly benefit from image-based modelling. The main contribution of this thesis work has been to bridge this gap between imaging and complex modelling. However, it is unlikely that there will be a 'one-for-all-solution' for image-based modelling. On the contrary, X-ray computed tomography is a complex technology with many work-steps and aspects. A 'one-for-all-solution' would often limit the quality of the results. We have therefore introduced the term XAE which proposes a holistic view on X-ray three-dimensional imaged-based modelling and acts as a framework for different tailored solutions.

Approaches within this project have been developed for non-crimp fabric reinforced, short fibre injection moulded, pultruded, and prepreg composites for glass, carbon as well as natural fibres. The applied load cases range from tension, compression, and fatigue to crash applications.

Image-based modelling is not, and will not become, the universal solution for material analysis and modelling. In some cases classical numerical modelling or modelling based on machine learning or deep neural networks might deliver more accurate, cheaper and

faster solutions. Further, it requires smart choices of method and parameters for image acquisition and reconstruction as well as tailored solutions for image analysis and modelling. However, the possible benefits are promising; failure mechanisms can be studied and implemented in models, in-situ strain fields can be used to validate models, or model-based scans of manufactured parts can assure safe operation.

I am therefore convinced that X-ray computed tomography three-dimensional image-based modelling will trigger enormous improvements in research, industrial development and production.

CHAPTER 6

Summary of appended papers

Summary Paper A

This study is one of the first that systematically transfers micro X-ray computed tomography data of fibre reinforced composites into a finite element models. This non-trivial process requires a holistic approach where all work-steps in imaging are aligned towards the modelling goal. Therefore, the expression X-ray computed tomography aided engineering (XAE) process has been coined. This process has been demonstrated on a non-crimp fabric glass fibre reinforced composite which is extensively used as material system for wind turbine blades. With the image-based models on the fibre and fibre bundle level the large scales properties of the wind turbine blades can be better understood and consequently lead to improved material systems. In particular, the blade stiffness and fatigue behaviour is of importance. With the presented automated image analysis schemes the tensile modulus of the scanned samples is accurately numerically predicted. Further, detailed stress analyses of critical regions in the bundle layup are conducted.

Summary Paper B

Paper B bases on the in **Paper A** developed image analysis, meshing and mapping strategies for non-crimp fabric glass fibre reinforced composites. Often, image analysis presents the bottleneck in the entire workflow from image acquisition to numerical model results. Designing an advanced algorithm for fibrous composites which is easy-applicable, accurate and fast is a challenging and time-consuming task. Depending on the modelling goal different image analysis methods are required. Here, two image analysis methodologies

are assessed based on their influence on the stress distributions in the fibre bundle structure. The methods differ in their representation of the boundary between fibre bundles. Both methods numerically predict stress concentrations in the overlapping area of off-axis backing and unidirectional bundles. The validation of accuracy of the stress levels remains for further research.

Summary Paper C

In **Paper C** new segmentation, mapping and modelling methods designed for non-crimp fabric glass fibre reinforced composites have been presented. The introduced structure tensor method for a fibre orientation analysis in combination with an advanced mapping scheme allows for accurate and fast modelling. Instead of several hours it has become a matter of minutes to equip a model with fibre orientations based on an X-ray computed tomography data-set. However, the methodology from **Paper A** has not only been refined but a new research field has been opened. This presented scheme has proven its robustness to low-resolution image data. Even though 99.8 % of the original data size has been removed the predicted numerical tensile modulus is only 4.7 % lower than compared to the model based on the high-resolution data. Thus, it can be stated that the model can accurately predict fibre orientations for a voxel-size of 64 µm, corresponding to approximately three times the fibre diameter.

Summary Paper D

The research direction opened in **Paper C** has been consequently pursued in this study. It exploits therefore the progress in imaging and image analysis to introduce for the first time an accurate, automated and fast fibre orientation image-based model of a full component in an industrial application. The studied sample is an injection moulded glass fibre reinforced polymer. With the applied robust structure tensor method for a low resolution of 60 µm in voxel-size fibre orientations can still be captured accurately and with the novel mapping method transferred into an automotive crash model. The image analysis and mapping process thereby creates a model based on approximately 210 million voxels for 43 thousand integration points. The entire process for the studied sample with a length of 20 cm takes approximately 10 minutes. Therefore, it is now possible to set-up an accurate X-ray computed tomography-based model of a full scale fibrous composite part in an industrial serial development in a matter of hours, including image acquisition, image analysis, and mapping.

Summary Paper E

Paper E emphasises the possibilities of novel X-ray imaging technologies. An ultra-fast small angle X-ray scattering tensor tomography procedure for synchrotron imaging has been successfully demonstrated as basis for image-based numerical modelling. A short carbon fibre reinforced polyether ether ketone composite cylindrical sample with a

diameter of 19 mm and a height of 14 mm has been investigated. Regular image-based models of carbon fibre reinforced composites require high-resolution image data with voxel-sizes up to 5 µm. The presented approach relies on a voxel-size of only 100 µm, approximately fifteen times the fibre diameter. This extreme low resolution created the demand for a novel modelling approach in order to accurately predict the tensile modulus. It goes therefore beyond classical fibre orientation mapping and computes an updated stiffness matrix based on sub-voxel fibre orientation distribution in combination with a local fibre volume fraction. Both parameters are calculated based on the reconstructed scattering tensor data. With the progress presented in this study the possible field of view for carbon fibre orientation image-based modelling is enlarged by three to six orders of magnitude compared to state of the art approaches.

Summary Paper F

Usually image data is much richer in information content than the final numerical model. Even though image analysis often represents the most time-consuming task in an X-ray computed tomography aided engineering analysis, it is the mapping process that decides how much of the original image information is transferred to the finite element model. With **Paper F** the importance of this process is underlined. Here, an open access algorithm in form of a Jupyter notebook is described which combines accurate and fast fibre orientation analysis with a mapping scheme. The fibre orientation analysis uses a structure tensor approach which computes a dominant fibre orientation per voxel in the image data. These fibre orientations are then mapped either element-wise or integration point-wise onto the target numerical model. This algorithm has been used in **Paper C** and demonstrated its excellence in terms of speed, accuracy and robustness to low-resolution image data.

References

[1] K. M. Jespersen et al. Fatigue damage assessment of uni-directional non-crimp fabric reinforced polyester composite using X-ray computed tomography. *Composites Science and Technology* **136** (2016), 94–103. DOI: 10.1016/j.compscitech.2016.10.006.

[2] O. Asumani and R. Paskaramoorthy. Fatigue and impact strengths of kenaf fibre reinforced polypropylene composites: effects of fibre treatments. *Advanced Composite Materials* **30** (2021), 103–115. DOI: 10.1080/09243046.2020.1733308.

[3] X. Hui, Y. Xu, and W. Zhang. An integrated modeling of the curing process and transverse tensile damage of unidirectional CFRP composites. *Composite Structures* **263** (2021), 113681. DOI: 10.1016/j.compstruct.2021.113681.

[4] S. M. Sisodia et al. Effects of voids on quasi-static and tension fatigue behaviour of carbon-fibre composite laminates. *Journal of Composite Materials* **49** (2015), 2137–2148. DOI: 10.1177/0021998314541993.

[5] H. Ghayoor et al. Numerical analysis of resin-rich areas and their effects on failure initiation of composites. *Composites Part A: Applied Science and Manufacturing* **117** (2019), 125–133. DOI: 10.1016/j.compositesa.2018.11.016.

[6] R. Talreja and A. M. Waas. Concepts and definitions related to mechanical behavior of fiber reinforced composite materials. *Composites Science and Technology* **217** (2022), 109081. DOI: 10.1016/j.compscitech.2021.109081.

[7] F. Stig and S. Hallström. Assessment of the mechanical properties of a new 3D woven fibre composite material. *Composites Science and Technology* **69** (2009), 1686–1692. DOI: 10.1016/j.compscitech.2008.04.047.

[8] C. Oddy et al. A framework for macroscale modelling of inelastic deformations in 3D-woven composites. *Mechanics of Materials* **160** (2021), 103856. DOI: 10.1016/j.mechmat.2021.103856.

[9] P. J. Liotier, A. Vautrin, and C. Delisée. Characterization of 3D morphology and microcracks in composites reinforced by multi-axial multi-ply stitched preforms. *Composites Part A: Applied Science and Manufacturing* **41** (2010), 653–662. DOI: 10.1016/j.compositesa.2010.01.015.

[10] M. Saeedifar et al. Damage assessment of NCF, 2D and 3D woven composites under compression after multiple-impact using acoustic emission. *Composites Part A: Applied Science and Manufacturing* **132** (2020), 105833. DOI: `10.1016/j.compositesa.2020.105833`.

[11] R. Joffe et al. Compressive failure analysis of non-crimp fabric composites with large out-of-plane misalignment of fiber bundles. *Composites Part A: Applied Science and Manufacturing* **36** (2005), 1030–1046. DOI: `10.1016/j.compositesa.2004.10.028`.

[12] A. Shipsha, S. Hallström, and M. Burman. Effect of stacking sequence and bundle waviness in quasi-isotropic NCF composites subjected to compression. *Composites Part B: Engineering* **178** (2019), 107423. DOI: `10.1016/j.compositesb.2019.107423`.

[13] R. M. Auenhammer et al. X-ray tomography based numerical analysis of stress concentrations in non-crimp fabric reinforced composites - assessment of segmentation methods. *IOP Conference Series: Materials Science and Engineering* **942** (2020), 012038. DOI: `10.1088/1757-899X/942/1/012038`.

[14] K. M. Jespersen et al. Fatigue damage assessment of uni-directional non-crimp fabric reinforced polyester composite using X-ray computed tomography. *Composites Science and Technology* **136** (2016), 94–103. DOI: `10.1016/j.compscitech.2016.10.006`.

[15] A. Prajapati et al. Observing the evolution of fatigue damage and associated strain fields in a correlative, multiscale 3D time-lapse study of quasi-unidirectional glass fibre composites. *IOP Conference Series: Materials Science and Engineering* **942** (2020), 012039. DOI: `10.1088/1757-899x/942/1/012039`.

[16] H. Lee and D. Cho. Effects of A, B, and S components on fiber length distribution, mechanical, and impact properties of carbon fiber/ABS composites produced by different processing methods. *Journal of Applied Polymer Science* **138** (2021), 50674. DOI: `10.1002/app.50674`.

[17] F. L. Guo et al. Modeling and characterizations of mechanical behaviors of short carbon fiber and short glass fiber reinforced polyetherimide composites. *Composites Science and Technology* **229** (2022), 109685. DOI: `10.1016/j.compscitech.2022.109685`.

[18] Z. Li et al. Multiscale modeling based failure criterion of injection molded SFRP composites considering skin-core-skin layered microstructure and variable parameters. *Composite Structures* **286** (2022), 115277. DOI: `10.1016/j.compstruct.2022.115277`.

[19] H. Wei et al. LS-DYNA Machine Learning – Based Multiscale Method for Nonlinear Modeling of Short Fiber – Reinforced Composites. *Journal of Engineering Mechanics* **149** (2023), 04023003. DOI: `10.1061/JENMDT.EMENG-6945`.

[20] M. R. Sanjay et al. Characterization and properties of natural fiber polymer composites: A comprehensive review. *Journal of Cleaner Production* **172** (2018), 566–581. DOI: `10.1016/j.jclepro.2017.10.101`.

[21] B. Madsen and E. K. Gamstedt. Wood versus Plant Fibers: Similarities and Differences in Composite Applications. *Advances in Materials Science and Engineering* **2013** (2013), 564346. DOI: `10.1155/2013/564346`.

[22] K. L. Pickering, M. G. A. Efendy, and T. M. Le. A review of recent developments in natural fibre composites and their mechanical performance. *Composites Part A: Applied Science and Manufacturing* **83** (2016), 98–112. DOI: 10.1016/j.compositesa.2015.08.038.

[23] S. Gokulkumar et al. Measuring Methods of Acoustic Properties and Influence of Physical Parameters on Natural Fibers: A Review. *Journal of Natural Fibers* **17** (2020), 1719–1738. DOI: 10.1080/15440478.2019.1598913.

[24] P. Peças et al. Natural Fibre Composites and Their Applications: A Review. *Journal of Composites Science* **2** (2018), 66. DOI: 10.3390/jcs2040066.

[25] M.-P. Ho et al. Critical factors on manufacturing processes of natural fibre composites. *Composites Part B: Engineering* **43** (2012), 3549–3562. DOI: 10.1016/j.compositesb.2011.10.001.

[26] V. Tojaga et al. Continuum damage micromechanics description of the compressive failure mechanisms in sustainable biocomposites and experimental validation. *Journal of the Mechanics and Physics of Solids* **171** (2023), 105138. DOI: 10.1016/j.jmps.2022.105138.

[27] J. Andersons et al. Strength distribution of elementary flax fibres. *Composites Part B: Engineering* **65** (2005), 693–702. DOI: 10.1016/j.compscitech.2004.10.001.

[28] C. Elanchezhian et al. Review on mechanical properties of natural fiber composites. *Materials Today: Proceedings* **5** (2018), 1785–1790. DOI: 10.1016/j.matpr.2017.11.276.

[29] S. Réquilé et al. Interfacial properties of hemp fiber / epoxy system measured by microdroplet test: Effect of relative humidity. *Composites Science and Technology* **181** (2019), 107694. DOI: 10.1016/j.compscitech.2019.107694.

[30] M. Chappell. *Principles of Medical Imaging for Engineers*. Springer International Publishing, 2020. DOI: 10.1007/978-3-030-30511-6.

[31] S. Garcea, Y. Wang, and P. Withers. X-ray computed tomography of polymer composites. *Composites Science and Technology* **156** (2018), 305–319. DOI: 10.1016/j.compscitech.2017.10.023.

[32] P. J. Withers et al. X-ray computed tomography. *Nature Reviews Methods Primers* **1** (2021), 18. DOI: 10.1038/s43586-021-00015-4.

[33] M. J. Turunen et al. Evaluation of composition and mineral structure of callus tissue in rat femoral fracture. *Journal of Biomedical Optics* **19** (2014), 025003. DOI: 10.1117/1.JBO.19.2.025003.

[34] A. Gustafsson et al. Linking multiscale deformation to microstructure in cortical bone using in situ loading, digital image correlation and synchrotron X-ray scattering. *Acta Biomaterialia* **69** (2018), 323–331. DOI: 10.1016/j.actbio.2018.01.037.

[35] M. Liebi et al. Small-angle X-ray scattering tensor tomography: Model of the three-dimensional reciprocal-space map, reconstruction algorithm and angular sampling requirements. *Acta Crystallographica Section A: Foundations and Advances* **74** (2018), 12–24. DOI: 10.1107/S205327331701614X.

[36] B. Chang et al. Microstructure characterization in a single isotactic polypropylene spherulite by synchrotron microfocus wide angle X-ray scattering. *Polymer* **142** (2018), 387–393. DOI: 10.1016/j.polymer.2018.03.061.

[37] A. S. Obdrup et al. Classifying condition of ultra-high-molecular-weight polyethylene ropes with wide-angle X-ray scattering. *Polymer Testing* **109** (2022), 107524. DOI: `10.1016/j.polymertesting.2022.107524`.

[38] A. Kupsch et al. Evolution of CFRP stress cracks observed by in-situ X-ray refractive imaging. *IOP Conference Series: Materials Science and Engineering* **942** (2020), 012035. DOI: `10.1088/1757-899X/942/1/012035`.

[39] H. Markrötter et al. A Review of X-Ray Imaging at the BAMline (BESSY II). *Advanced Engineering Materials* (2023), 2201034. DOI: `10.1002/adem.202201034`.

[40] A. Olivo. Edge-illumination x-ray phase-contrast imaging. *Journal of Physics: Condensed Matter* **33** (2021), 363002. DOI: `10.1088/1361-648X/ac0e6e`.

[41] J. Vila-Comamala et al. High sensitivity X-ray phase contrast imaging by laboratory grating-based interferometry at high Talbot order geometry. *Optics Express* **29** (2021), 2049–2064. DOI: `10.1364/OE.414174`.

[42] E. Maire and P. J. Withers. Quantitative X-ray tomography. *International Materials Reviews* **59** (2014), 1–43. DOI: `10.1179/1743280413Y.0000000023`.

[43] H. Villarraga-Gómez, E. L. Herazo, and S. T. Smith. X-ray computed tomography: from medical imaging to dimensional metrology. *Precision Engineering* **60** (2019), 544–569. DOI: `10.1016/j.precisioneng.2019.06.007`.

[44] *The ASTRA Toolbox*. `https://www.astra-toolbox.com/`. Accessed: 2020-10-06.

[45] R. Chang and J. W. J. Thoman. *Physical Chemistry for the Chemical Sciences*. University Science Books, Canada, 2015.

[46] K. J. Batenburg and L. Plantagie. Fast approximation of algebraic reconstruction methods for tomography. *IEEE Transactions on Image Processing* **21** (2012), 3648–3658. DOI: `10.1109/TIP.2012.2197012`.

[47] M. Akagi et al. Deep learning reconstruction improves image quality of abdominal ultra-high-resolution CT. *European Radiology* **29** (2019), 6163–6171. DOI: `10.1007/s00330-019-06170-3`.

[48] J. Fu, J. Dong, and F. Zhao. A Deep Learning Reconstruction Framework for Differential Phase-Contrast Computed Tomography with Incomplete Data. *IEEE Transactions on Image Processing* **29** (2020), 2190–2202. DOI: `10.1109/TIP.2019.2947790`.

[49] M. van Eijnatten et al. 3D deformable registration of longitudinal abdominopelvic CT images using unsupervised deep learning. *Computer Methods and Programs in Biomedicine* **208** (2021), 106261. DOI: `10.1016/j.cmpb.2021.106261`.

[50] E. A. Casanova et al. SAXS imaging reveals optimized osseointegration properties of bioengineered oriented 3D-PLGA/aCaP scaffolds in a critical size bone defect model. *Biomaterials* **294** (2023), 121989. DOI: `10.1016/j.biomaterials.2022.121989`.

[51] O. Bunk et al. Multimodal x-ray scatter imaging. *New Journal of Pysics* **11** (2009), 123016. DOI: `10.1088/1367-2630/11/12/123016`.

[52] B. R. Pauw et al. Extending synchrotron SAXS instrument ranges through addition of a portable , inexpensive USAXS module with vertical rotation axes. *Journal of Synchrotron Radiation* **28** (2021), 824–833. DOI: `10.1107/S1600577521003313`.

[53] D. J. Kaspersen et al. Small-Angle X-ray Scattering Demonstrates Similar Nanostructure in Cortical Bone from Young Adult Animals of Different Species. *Calcified Tissue International* **99** (2016), 76–87. DOI: `10.1007/s00223-016-0120-z`.

[54] A. Rodriguez-Palomo et al. In Situ Visualization of the Structural Evolution and Alignment of Lyotropic Liquid Crystals in Confined Flow. *Small* **17** (2021), 2006229. DOI: `10.1002/smll.202006229`.

[55] M. Kagias et al. Dual phase grating interferometer for tunable dark-field sensitivity. *Applied Physics Letters* **110** (2017), 014105. DOI: `10.1063/1.4973520`.

[56] M. Kagias et al. Diffractive small angle X-ray scattering imaging for anisotropic structures. *Nature Communications* **10** (2019), 5130. DOI: `10.1038/s41467-019-12635-2`.

[57] J. Kim et al. X-ray scattering tensor tomography with circular gratings. *Applied Physics Letters* **116** (2020), 134102. DOI: `10.1063/1.5145361`.

[58] J. Kim et al. Macroscopic mapping of microscale fibers in freeform injection molded fiber-reinforced composites using X-ray scattering tensor tomography. *Composites Part B: Engineering* **233** (2022), 109634. DOI: `10.1016/j.compositesb.2022.109634`.

[59] I. Belevich et al. Microscopy Image Browser: A Platform for Segmentation and Analysis of Multidimensional Datasets. *PloS Biology* **14** (2016), e1002340. DOI: `10.1371/journal.pbio.1002340`.

[60] I. Arganda-Carreras et al. Trainable Weka Segmentation: A machine learning tool for microscopy pixel classification. *Bioinformatics* **33** (2017), 2424–2426. DOI: `10.1093/bioinformatics/btx180`.

[61] R. M. Auenhammer et al. Automated X-ray computer tomography segmentation method for finite element analysis of non-crimp fabric reinforced composites. *Composite Structures* **256** (2021), 113136. DOI: `10.1016/j.compstruct.2020.113136`.

[62] P.-S. Ho, Y.-S. Hwang, and H.-Y. Tsai. Machine learning framework for automatic image quality evaluation involving a mammographic American College of Radiology phantom. *Physica Medica* **102** (2022), 1–8. DOI: `10.1016/j.ejmp.2022.08.004`.

[63] H. Barnes et al. Machine learning in radiology: the new frontier in interstitial lung diseases. *The Lancet Digital Health* **5** (2023), e41–e50. DOI: `10.1016/S2589-7500(22)00230-8`.

[64] N. Jeppesen et al. Quantifying effects of manufacturing methods on fiber orientation in unidirectional composites using structure tensor analysis. *Composites Part A: Applied Science and Manufacturing* **149** (2021), 106541. DOI: `10.1016/j.compositesa.2021.106541`.

[65] *Avizo Software*. `https://www.thermofisher.com/se/en/home/electron-microscopy/products/software-em-3d-vis/avizo-software.html`. Accessed: 2023-04-07.

[66] *Simpleware Software Solutions*. `https://www.synopsys.com/simpleware.html`. Accessed: 2023-04-07.

[67] *Retomo*. `https://www.beta-cae.com/retomo.htm`. Accessed: 2023-04-07.

[68] *Fiji-ImageJ*. `https://imagej.net/software/fiji/`. Accessed: 2023-04-07.

[69] *ImageJ - Trackmate*. `https://imagej.net/plugins/trackmate/`. Accessed: 2023-04-07.

[70] *ImageJ - Trainable Weka Segmentation*. `https://imagej.net/plugins/tws/`. Accessed: 2023-04-07.

[71] *The Software for the Practical Analysis of Materials.* `https://ttk.gricad-pages.univ-grenoble-alpes.fr/spam/intro.html`. Accessed: 2023-04-07.

[72] U. A. Mortensen et al. The impact of the fiber volume fraction on the fatigue performance of glass fiber composites. *Composites Part A: Applied Science and Manufacturing* **169** (2023), 107493. DOI: `10.1016/j.compositesa.2023.107493`.

[73] M. J. Emerson et al. Individual fibre segmentation from 3D X-ray computed tomography for characterising the fibre orientation in unidirectional composite materials. *Composites Part A: Applied Science and Manufacturing* **97** (2017), 83–92. DOI: `10.1016/j.compositesa.2016.12.028`.

[74] M. J. Emerson et al. Quantifying fibre reorientation during axial compression of a composite through time-lapse X-ray imaging and individual fibre tracking. *Composites Science and Technology* **168** (2018), 47–54. DOI: `10.1016/j.compscitech.2018.08.028`.

[75] M. Krause et al. Determination of the fibre orientation in composites using the structure tensor and local X-ray transform. *Journal of Materials Science* **45** (2010), 888–896. DOI: `10.1007/s10853-009-4016-4`.

[76] I. Straumit, S. V. Lomov, and M. Wevers. Quantification of the internal structure and automatic generation of voxel models of textile composites from X-ray computed tomography data. *Composites Part A: Applied Science and Manufacturing* **69** (2015), 150–158. DOI: `10.1016/j.compositesa.2014.11.016`.

[77] N. Jeppesen et al. Characterization of the fiber orientations in non-crimp glass fiber reinforced composites using structure tensor. *IOP Conference Series: Materials Science and Engineering* **942** (2020), 012037. DOI: `10.1088/1757-899x/942/1/012037`.

[78] *Structure Tensor for Python.* `https://pypi.org/project/structure-tensor/`. Accessed: 2023-04-07.

[79] R. M. Auenhammer et al. Robust numerical analysis of fibrous composites from X-ray computed tomography image data enabling low resolutions. *Composites Science and Technology* **224** (2022), 109458. DOI: `10.1016/j.compscitech.2022.109458`.

[80] D. Wilhelmsson et al. Influence of in-plane shear on kink-plane orientation in a unidirectional fibre composite. *Composites Part A: Applied Science and Manufacturing* **119** (2019), 283–290. DOI: `10.1016/j.compositesa.2019.01.018`.

[81] R. M. Sencu et al. Multiscale image-based modelling of damage and fracture in carbon fibre reinforced polymer composites. *Composites Science and Technology* **198** (2020), 108243. DOI: `10.1016/j.compscitech.2020.108243`.

[82] B. Wintiba et al. Automated reconstruction and conformal discretization of 3D woven composite CT scans with local fiber volume fraction control. *Composite Structures* **248** (2020), 112438. DOI: `10.1016/j.compstruct.2020.112438`.

[83] J. Ryatt and M. Ramulu. Finite Elements in Analysis & Design Numerical investigation of the application of voxel based meshes for stochastic tow based discontinuous composites. *Finite Elements in Analysis & Design* **214** (2023), 103874. DOI: `10.1016/j.finel.2022.103874`.

[84] S. Yu, D. Zhang, and K. Qian. Numerical Analysis of Macro-Scale Mechanical Behaviors of 3D Orthogonal Woven Composites using a Voxel-Based Finite Element

Model. *Applied Composite Materails* **26** (2019), 65–83. DOI: `10.1007/s10443-018-9707-z`.

[85] A. Doitrand et al. Comparison between voxel and consistent meso-scale models of woven composites. *Composites Part A: Applied Science and Manufacturing* **73** (2015), 143–154. DOI: `10.1016/j.compositesa.2015.02.022`.

[86] N. Naouar et al. Meso-FE modelling of textile composites and X-ray tomography. *Journal of Materials Science* **55** (2020), 16969–16989. DOI: `10.1007/s10853-020-05225-x`.

[87] A. Ewert et al. Predicting the overall response of an orthogonal 3D woven composite using simulated and tomography-derived geometry. *Composite Structures* **243** (2020), 112169. DOI: `10.1016/j.compstruct.2020.112169`.

[88] M. Schneider. A review of nonlinear FFT-based computational homogenization methods. *Acta Mechanica* **232** (2021), 2051–2100. DOI: `10.1007/s00707-021-02962-1`.

[89] M. Kabel, D. Merkert, and M. Schneider. Use of composite voxels in FFT-based homogenization. *Computer Methods in Applied Mechanics and Engineering* **294** (2015), 168–188. DOI: `10.1016/j.cma.2015.06.003`.

[90] M. Iversen and A. Årmann. Characterisation of natural fibre composites using X-ray computer tomography aided engineering. *Master's Thesis, Chalmers University of Technology* (2023).

[91] I. Straumit et al. Identification of the flax fibre modulus based on an impregnated quasi-unidirectional fibre bundle test and X-ray computed tomography. *Composites Science and Technology* **151** (2017), 124–130. DOI: `10.1016/j.compscitech.2017.07.029`.

[92] Kang Li et al. Optimal Surface Segmentation in Volumetric Images-A Graph-Theoretic Approach. *IEEE Transactions on Pattern Analysis and Machine Intelligence* **28** (2006), 119–134. DOI: `10.1109/TPAMI.2006.19`.

[93] N. Jeppesen et al. "Sparse Layered Graphs for Multi-Object Segmentation". *2020 IEEE/CVF Conference on Computer Vision and Pattern Recognition (CVPR)*. IEEE, June 2020, pp. 12774–12782. DOI: `10.1109/CVPR42600.2020.01279`.

[94] D. Wilhelmsson et al. Compressive strength assessment of fibre composites based on a defect severity model. *Composites Science and Technology* **181** (2019), 107685. DOI: `10.1016/j.compscitech.2019.107685`.

[95] S. L. Omairey, P. D. Dunning, and S. Sriramula. Development of an ABAQUS plugin tool for periodic RVE homogenisation. *Engineering with Computers* **35** (2019), 567–577. DOI: `10.1007/s00366-018-0616-4`.

[96] C. C. Chamis. Simplified composite micromechanics equations for hygral, thermal and mechanical properties. *Ann. Conf. of the Society of the Plastics Industry (SPI) Reinforced Plastics/Composites Inst.* (1983), No. NASA–TM–83320.

[97] T. Mori and K. Tanaka. Average stress in matrix and average elastic energy of materials with misfitting inclusions. *Acta Metallurgica* **21** (1973), 571–574. DOI: `10.1016/0001-6160(73)90064-3`.

[98] Y. Benveniste. A new approach to the application of Mori-Tanaka's theory in composite materials. *Mechanics of Materials* **6** (1987), 147–157. DOI: `10.1016/0167-6636(87)90005-6`.

[99] Y. Benveniste, G. J. Dvorak, and T. Chen. On diagonal and elastic symmetry of the approximate effective stiffness tensor of heterogeneous media. *Journal of the Mechanics and Physics of Solids* **39** (1991), 927–946. DOI: 10.1016/0022-5096(91)90012-D.

[100] J. D. Eshelby. The determination of the elastic field of an ellipsoidal inclusion, and related problems. *Proceedings of the Royal Society of London. Series A, Mathematical and Physical Science* **241** (1957), 376–396.

[101] S. G. Advani and C. L. Tucker. The Use of Tensors to Describe and Predict Fiber Orientation in Short Fiber Composites. *Journal of Rheology* **31** (1987), 751–784. DOI: 10.1122/1.549945.